

**Detection of Deuterated Hydrocarbon Nanoparticles in the Whirlpool Galaxy, M51**

B. T. DRAINE,<sup>1</sup> KARIN SANDSTROM,<sup>2</sup> DANIEL A. DALE,<sup>3</sup> J.-D. T. SMITH,<sup>4</sup> RYAN CHOWN,<sup>5</sup>  
 GRANT P. DONNELLY,<sup>6</sup> SARA E. DUVAL,<sup>4</sup> CORY M. WHITCOMB,<sup>4</sup> ANGELA ADAMO,<sup>7</sup> L. ARMUS,<sup>8</sup>  
 DANIELLE A. BERG,<sup>9</sup> TORSTEN BÖKER,<sup>10</sup> ALBERTO D. BOLATTO,<sup>11,12</sup> MARTHA L. BOYER,<sup>13</sup>  
 DANIELA CALZETTI,<sup>14</sup> B. G. ELMEGREEN,<sup>15</sup> BRANDT A. L. GACHES,<sup>16</sup> KARL D. GORDON,<sup>13</sup>  
 L. K. HUNT,<sup>17</sup> R. C. KENNICUTT,<sup>18,19</sup> RALF S. KLESSSEN,<sup>20,21,22,23</sup> THOMAS S.-Y. LAI,<sup>8</sup>  
 ADAM K. LEROY,<sup>5,24</sup> SEAN T. LINDEN,<sup>25</sup> ALEX PEDRINI,<sup>26</sup> NOAH S. J. ROGERS,<sup>27,28</sup>  
 JULIA C. ROMAN-DUVAL,<sup>13</sup> EVA SCHINNERER,<sup>29</sup> EVAN B. SKILLMAN,<sup>30</sup> FABIAN WALTER,<sup>29</sup>  
 TONY D. WEINBECK,<sup>3</sup> AND BENJAMIN F. WILLIAMS<sup>31</sup>

<sup>1</sup>*Dept. of Astrophysical Sciences, Princeton University, Princeton, NJ 08544, USA*

<sup>2</sup>*Department of Astronomy and Astrophysics, University of California San Diego, 9500 Gilman Drive, La Jolla, CA 92093, USA*

<sup>3</sup>*Department of Physics and Astronomy, University of Wyoming, Laramie, WY 82071, USA*

<sup>4</sup>*Dept. of Physics and Astronomy, University of Toledo, Toledo, OH 43606, USA*

<sup>5</sup>*Department of Astronomy, The Ohio State University, 140 West 18th Avenue, Columbus, OH 43210, USA*

<sup>6</sup>*Ritter Astrophysical Research Center, University of Toledo, Toledo, OH 43606, USA*

<sup>7</sup>*The Oskar Klein Centre, Department of Astronomy, Stockholm University, AlbaNova, SE-106 91 Stockholm, Sweden*

<sup>8</sup>*IPAC, California Institute of Technology, 1200 E. California Blvd., Pasadena, CA 91125, USA*

<sup>9</sup>*Department of Astronomy, The University of Texas at Austin, 2515 Speedway, Stop C1400, Austin, TX 78712, USA*

<sup>10</sup>*European Space Agency, Space Telescope Science Institute, Baltimore, MD, USA*

<sup>11</sup>*Department of Astronomy, University of Maryland, College Park, MD 20742, USA*

<sup>12</sup>*Joint Space-Science Institute, University of Maryland, College Park, MD 20742, USA*

<sup>13</sup>*Space Telescope Science Institute, 3700 San Martin Drive, Baltimore, MD 21218, USA*

<sup>14</sup>*Department of Astronomy, University of Massachusetts, Amherst, MA 01002, USA*

<sup>15</sup>*Katonah, NY 10536, USA*

<sup>16</sup>*Department of Space, Earth and Environment, Chalmers University of Technology, Gothenburg SE-412 96, Sweden*

<sup>17</sup>*INAF - Osservatorio Astrofisico di Arcetri, Largo E. Fermi 5, 50125 Firenze, Italy*

<sup>18</sup>*Steward Observatory, University of Arizona, Tucson, AZ 85721-0065, USA*

<sup>19</sup>*Mitchell Institute for Fundamental Physics and Astronomy, Texas A&M University, College Station, TX 77843-4242, USA*

<sup>20</sup>*Universität Heidelberg, Zentrum für Astronomie, Institut für Theoretische Astrophysik, Albert-Ueberle-Str. 2, 69120 Heidelberg, Germany*

<sup>21</sup>*Universität Heidelberg, Interdisziplinäres Zentrum für Wissenschaftliches Rechnen, Im Neuenheimer Feld 225, 69120 Heidelberg, Germany*

<sup>22</sup>*Harvard-Smithsonian Center for Astrophysics, 60 Garden Street, Cambridge, MA 02138, U.S.A.*

<sup>23</sup>*Elizabeth S. and Richard M. Cashin Fellow at the Radcliffe Institute for Advanced Studies at Harvard University, 10 Garden Street, Cambridge, MA 02138, U.S.A.*

<sup>24</sup>*Center for Cosmology and Astroparticle Physics (CCAPP), 191 West Woodruff Avenue, Columbus, OH 43210, USA*

<sup>25</sup>*Steward Observatory, University of Arizona, 933 N Cherry Avenue, Tucson, AZ 85721, USA*

<sup>26</sup>*Department of Astronomy, Oskar Klein center, Stockholm University, AlbaNova, SE-106 91 Stockholm, Sweden*

<sup>27</sup>*Department of Physics and Astronomy, Northwestern University, 2145 Sheridan Road, Evanston, IL 60208, USA*

<sup>28</sup>Center for Interdisciplinary Exploration and Research in Astrophysics (CIERA), Northwestern University, 1800 Sherman Avenue, Evanston, IL 60201, USA

<sup>29</sup>Max Planck Institut für Astronomie, Königstuhl 17, D-69117, Heidelberg, Germany

<sup>30</sup>University of Minnesota, Minnesota Institute for Astrophysics, School of Physics and Astronomy, 116 Church Street S.E., Minneapolis, MN 55455, USA

<sup>31</sup>Astronomy Department, University of Washington, Seattle, WA 98195, USA

## ABSTRACT

Deuteration of hydrocarbon material, including polycyclic aromatic hydrocarbons (PAHs), has been proposed to account for the low gas-phase abundances of D in the interstellar medium (ISM). JWST spectra of four star-forming regions in M51 show an emission feature, with central wavelength  $\sim 4.647\mu\text{m}$  and FWHM  $0.0265\mu\text{m}$ , corresponding to the C–D stretching mode in aliphatic hydrocarbons. The emitting aliphatic material is estimated to have  $(\text{D}/\text{H})_{\text{aliph}} \approx 0.17 \pm 0.02$  – a factor  $\sim 10^4$  enrichment relative to the overall ISM. On  $\sim 50$  pc scales, deuteration levels toward four H II regions in M51 are 2–3 times higher than in the Orion Bar photodissociation region (PDR), with implications for the processes responsible for the formation and evolution of hydrocarbon nanoparticles, including PAHs. The deuteration of the aliphatic material is found to anticorrelate with helium ionization in the associated H II, suggesting that harsh FUV radiation may act to lower the deuteration of aliphatics in PDRs near massive stars. No evidence is found for deuteration of aromatic material, with  $(\text{D}/\text{H})_{\text{arom}} \lesssim 0.016$ : deuteration of the aliphatic material exceeds that of the aromatic material by at least a factor 10. The observed levels of deuteration may account for the depletion of D observed in the Galactic ISM. If so, the  $4.65\mu\text{m}$  feature may be detectable in absorption.

*Keywords:* ISM: abundances; ISM: dust, extinction; ISM: HII regions; ISM: lines and bands; ISM: PDRs; galaxies: ISM; galaxies: individual (M51); radiative transfer (1335)

## 1. INTRODUCTION

The abundance of deuterium provides key insights into many phenomena, ranging from nucleosynthesis in the early Universe to processes in the interstellar medium (ISM). Absorption line studies of gas at high redshift find  $\text{D}/\text{H} \approx (25.5 \pm 0.3)$  ppm, consistent with the predictions of Big Bang nucleosynthesis (Yeh et al. 2021, and references therein). Absorption line studies of gas-phase deuterium in the ISM find  $(\text{D}/\text{H})_{\text{gas}}$  as high as 23 ppm (Linsky et al. 2006), consistent with the expected small reduction in D/H by the stellar processing (“astration”) that has enriched the ISM with heavy elements. However, careful absorption line studies (Jenkins et al. 1999) discovered spatial variability in  $(\text{D}/\text{H})_{\text{gas}}$ , with very low  $(\text{D}/\text{H})_{\text{gas}} = 7.4^{+1.9}_{-1.3}$  ppm in the diffuse gas toward  $\delta\text{Ori}$ . Low values of  $(\text{D}/\text{H})_{\text{gas}}$  have since been observed on many Galactic sightlines, with  $(\text{D}/\text{H})_{\text{gas}} \approx 18$  ppm in the nearby ISM, and  $\sim 8.6 \pm 0.8$  ppm for a number of sightlines with  $5 \times 10^{20} \lesssim N_{\text{H}} \lesssim 2 \times 10^{21} \text{ cm}^{-2}$  (Linsky et al. 2006). A recent study by Friedman et al. (2023) has several sightlines with  $(\text{D}/\text{H})_{\text{gas}} < 9$  ppm. Remarkably, as much as 2/3 of the D is missing from the gas phase in some diffuse regions.

It has been conjectured that the “missing” D – up to  $\sim 14$  ppm with respect to H – has been incorporated into hydrocarbon grains (Jura 1982; Draine 2004, 2006), presumably including the polycyclic aromatic hydrocarbon (PAH) population. Deuterated hydrocarbons would have emission features in the  $4.3 - 4.7\mu\text{m}$  range due to the C–D stretching mode (Allamandola et al. 1989; Allamandola 1993).

Verstraete et al. (1996) found an unidentified emission band at  $4.65\mu\text{m}$  in the ISO-SWS spectrum of the M17 photodissociation region (PDR), and Peeters et al. (2004) reported emission bands at

4.4 $\mu\text{m}$  (present at  $1.9\sigma$  level) and 4.65 $\mu\text{m}$  (present at  $4.4\sigma$  level) in the ISO-SWS spectrum of the Orion Bar, identifying them as C–D stretching modes of deuterated PAHs.

AKARI spectra of a molecular cloud in the LMC showed an unidentified dust emission feature at 4.65 $\mu\text{m}$  (Boulanger et al. 2011). Doney et al. (2016) used AKARI spectra of Galactic H II regions to search for deuterated PAHs. In 6 of 53 targets, features were seen (at 4.63 $\mu\text{m}$  and 4.75 $\mu\text{m}$ ) that were attributed to aliphatic C–D stretching modes in PAHs, but interpretation was difficult due to blending with strong emission lines observed with the limited spectral resolution  $R \approx 100$  of AKARI. Onaka et al. (2022) reported an emission feature at 4.4 $\mu\text{m}$ , which they attributed to the aromatic C–D stretch, in the AKARI spectrum of a massive young stellar object.

Boersma et al. (2023) analyzed JWST spectra of a number of Galactic sources, confirming the 4.65 $\mu\text{m}$  emission feature in M17, with FWHM  $\approx 0.02\mu\text{m}$ . Peeters et al. (2024) verified this feature in JWST spectra of the Orion Bar PDR, with central wavelength  $\lambda_0 \approx 4.645\mu\text{m}$ , and reported tentative detection of emission at 4.35 $\mu\text{m}$  that they attributed to aromatic C–D.

The unprecedented sensitivity and excellent spectral resolution of JWST (Gardner et al. 2023) enable us to search in the Whirlpool galaxy (M51) for evidence that deuterium is sequestered in hydrocarbon nanoparticles. Here we report spectra<sup>1</sup> of four star-forming regions. All show an emission feature near 4.65 $\mu\text{m}$ , attributable to the aliphatic C–D stretch. After correcting for the complex gas-phase emission spectrum in this wavelength range, we find that all four regions are well fitted by a common band profile, with central wavelength  $\lambda_0 \approx 4.647\mu\text{m}$  and FWHM = 0.0265 $\mu\text{m}$ . This profile is consistent with observations of the Orion Bar. Relative to the 3.4 $\mu\text{m}$  emission feature, the aliphatic C–D feature is 2–3 times stronger in M51 than in the Orion Bar, indicating a higher degree of deuteration.

Our spectra show no evidence of any feature near 4.40 $\mu\text{m}$  as would be expected for the aromatic C–D stretch, nor do we see evidence of a suggested aliphatic feature near 4.75 $\mu\text{m}$ .

Our observations are reported in Section 2. The effects of deuteration are reviewed in Section 3. Section 4 describes modeling of the gas-phase emission (and absorption) that must be allowed for to extract the emission feature. Our results are presented and discussed in Section 5, and summarized in Section 6.

## 2. OBSERVATIONS

### 2.1. M51

Three regions of M51 have been spectroscopically mapped from 1–28  $\mu\text{m}$  as part of the Cycle 2 JWST M51 Treasury (GO 3435) using JWST NIRSpec (Jakobsen et al. 2022; Böker et al. 2022) and MIRI-MRS (Argyriou et al. 2023). The NIRSpec observations used the medium resolution grating/filter combinations G140M/F100LP, G235M/F170LP, and G395M/F290LP to obtain spectral resolution  $R \sim 1000$ . Each region was covered with four individual pointings to create a small strip that cuts across the spiral arm, with four dither positions per pointing. To remove stray light from open Micro-Shutter Assembly (MSA) shutters, we obtained a “leakcal” observation at every dither position for NIRSpec.

A full description of the observational program and data reduction will be presented in an upcoming paper (D.A. Dale et al. 2025, in preparation). In brief, we downloaded the `uncal` files from the Mikulski Archive for Space Telescopes (MAST) and reduced them with the JWST pipeline. For NIRSpec, we used version 1.16.1.dev14 of the pipeline (which allows for  $1/f$  noise removal from both the science and leakcal observations) with CRDS `jwst.1293.pmap`. We processed the observations through the Detector1 pipeline, including  $1/f$  noise correction with the `clean_flicker_noise` step. We then processed the data through the Spec2 and Spec3 pipeline stages, including the “leakcal” subtraction, and created drizzled cubes with 0''.05 pixels for each grating/filter combination.

<sup>1</sup> All wavelengths in this paper are rest frame, *in vacuo*.

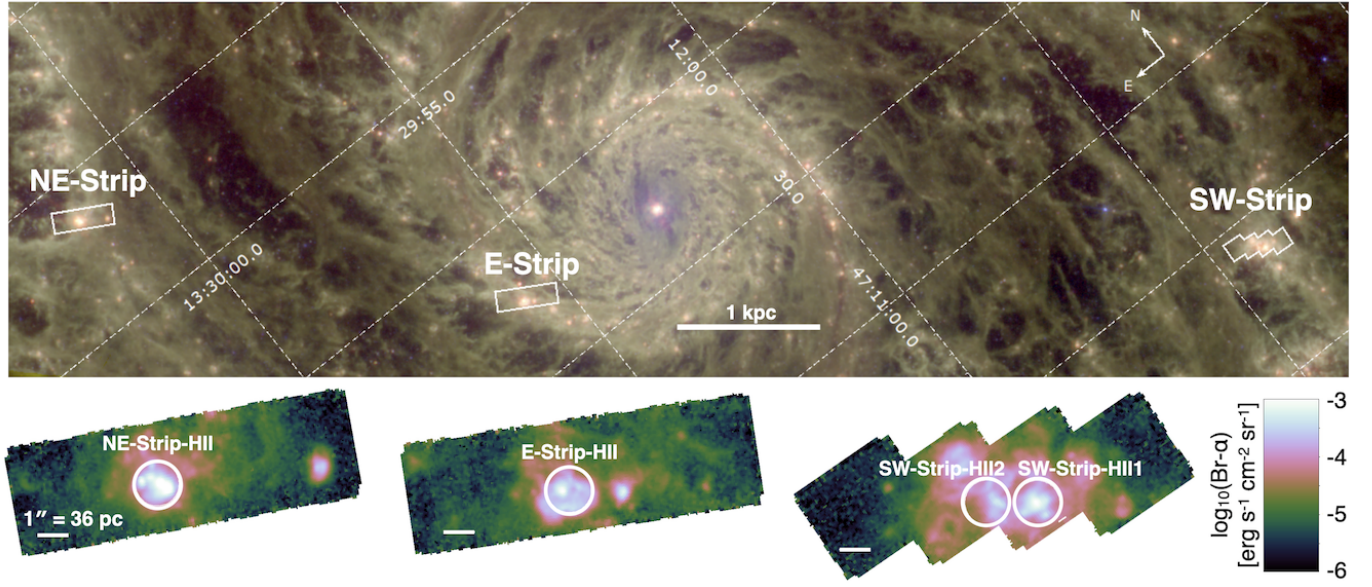


**Figure 1.** Image of a portion of M51; RGB=F1800W/F1130W/F560W ( $18\mu\text{m}$ ,  $11.3\mu\text{m}$ ,  $5.6\mu\text{m}$ ). Areas where we have obtained complete  $1 - 28\mu\text{m}$  spectroscopy are indicated. Expanded cutouts are Br $\alpha$  ( $4.05\mu\text{m}$ ) images of these areas. Spectra have been extracted for the four  $r = 0.75''$  circular regions shown in the cutouts.

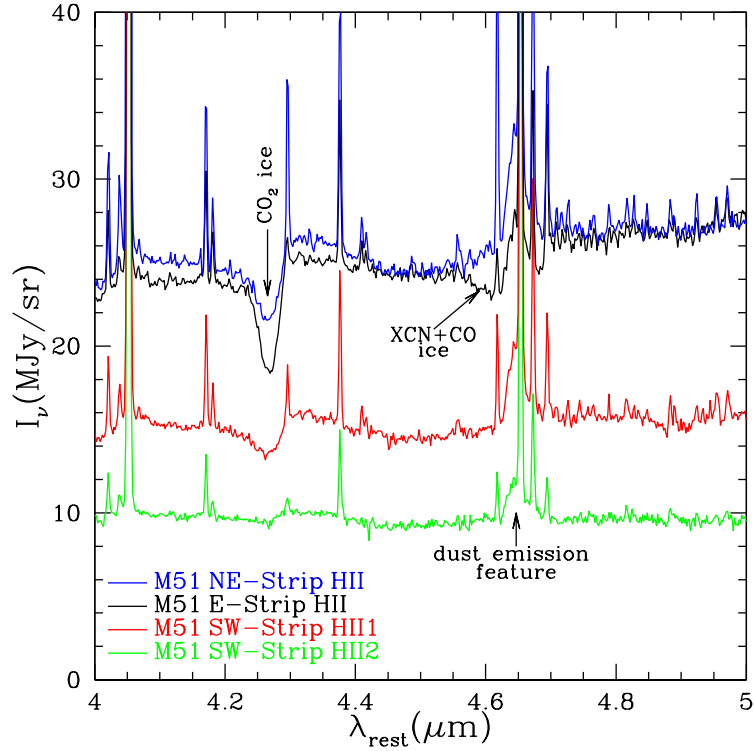


**Figure 2.**  $4 - 5\mu\text{m}$  spectra ( $R \approx 1100$ ) of four star-forming regions in M51 (see text). Observed wavelengths have been corrected for redshift (see Table 1 for adopted radial velocities). Three of the spectra show  $\text{CO}_2$  ice absorption (strongest in E-Strip H II). The E-Strip H II spectrum also shows  $4.56\text{--}4.69\mu\text{m}$  XCN+CO ice absorption. A dust emission feature near  $4.65\mu\text{m}$  is present in all spectra.



We extracted spectra in four  $r = 0''.75$  ( $\sim 27$  pc at the 7.5 Mpc distance of M 51) circular apertures targeting H II regions, shown in Figure 1, from each individual cube, propagating uncertainties from the pipeline-generated error cube. The  $r = 0''.75$  size is large compared to the point-spread function at  $\lambda < 5\mu\text{m}$ , so we have not convolved the cubes to a matched angular resolution. To stitch the spectra from each cube together, we calculated additive offsets (typically  $\sim 0.1$  MJy sr $^{-1}$ ) between the segments in their overlapping spectral regions and tied all orders to the G140M spectrum. In these bright star-forming regions, the results are not sensitive to the stitching approach.

The  $4 - 5\mu\text{m}$  spectra are shown in Figure 2. Strong emission lines are present, including H and He recombination lines. Three of the four spectra show clear evidence of absorption near  $4.26\mu\text{m}$  due to CO $_2$  ice. The E-Strip H II spectrum also shows an absorption feature near  $4.6\mu\text{m}$  attributed to “XCN” ice. All four spectra show a dust emission feature near  $4.65\mu\text{m}$ , but the spectra are complicated by strong emission lines: H 7-5 Pf  $\beta$   $4.654\mu\text{m}$ , multiplets from He I  $1s7\ell \rightarrow 1s5\ell'$  transitions (e.g.,  $1s7d \rightarrow 1s5f$   $^3F_4$   $4.642\mu\text{m}$ ), and multiplets from He I  $1s5\ell \rightarrow 1s4p$  transitions (e.g.,  $1s5s \rightarrow 1s4p$   $^3P_2$   $4.695\mu\text{m}$ ).

## 2.2. Orion Bar and M17

For comparison with M51, NIRSpec spectra (high resolution) of the Orion Bar (“atomic PDR” and “DF1”; Peeters et al. 2024) were obtained from <https://cdsarc.cds.unistra.fr/viz-bin/cat/J/A+A/685/A74>, and medium resolution NIRSpec spectra (x1d full aperture extractions) of M17 (“M17-PDR” and “M17B-PDR”; Boersma et al. 2023) were obtained from MAST <https://mast.stsci.edu>.

## 3. DEUTERATION OF HYDROCARBONS

C–D and C–H have identical interatomic potentials. Because of the mass difference, the vibrational frequencies for C–D stretching and bending modes are lower than for C–H. For free-flying CD and CH molecules, the difference in reduced masses gives  $\lambda_{\text{CD}}/\lambda_{\text{CH}} \approx \sqrt{13/7} = 1.363$ . With the observed aromatic C–H stretch in PAHs at  $\lambda_{\text{arom.CH}} = 3.29\mu\text{m}$ , and the C–H stretch in aliphatic material at  $\lambda_{\text{aliph.CH}} \approx 3.42\mu\text{m}$ , the deuterated counterparts are expected to be near  $\lambda_{\text{arom.CD}} \approx 4.48\mu\text{m}$  and  $\lambda_{\text{aliph.CD}} \approx 4.66\mu\text{m}$ . More detailed studies estimate  $\lambda_{\text{arom.CD}} \approx 4.40\mu\text{m}$  and  $\lambda_{\text{aliph.CD}} \approx 4.65\mu\text{m}$  (Bauschlicher et al. 1997; Hudgins et al. 2004; Yang et al. 2020; Yang & Li 2023a, V. J. Esposito 2024, private communication).

Because the zero-point energy in stretching and bending modes is lower for CD than for CH, the bond energy is greater by  $\sim 0.083$  eV (Draine 2006). With CD energetically favored over CH, one might expect interstellar hydrocarbons to have D/H ratios larger than  $(\text{D}/\text{H})_{\text{gas}}$ .

## 4. MODELING THE OBSERVED EMISSION

### 4.1. Recombination Lines and Reddening

Our goal is to examine the spectra for evidence of emission from deuterated hydrocarbons in M51. In addition to our spectra of four star-forming regions in M51, for comparison we apply the same analysis to spectra of the “atomic PDR” and “Dissociation Front 1” (“DF1”) positions in the Orion Bar PDR (Peeters et al. 2024), and two positions in the M17 PDR (Boersma et al. 2023).

We model the observed spectra as line emission plus dust emission attenuated by a foreground screen of dust with ices, and gas-phase CO:

$$I_\nu(\lambda) = I_\nu^{\text{line}} \exp [-(\tau_\lambda^{\text{dust}} + \tau_\lambda^{\text{ice}})] + (I_\nu^{\text{cont}} + I_\nu^{\text{CD}}) \exp [-(\tau_\lambda^{\text{dust}} + \tau_\lambda^{\text{ice}} + \tau_\lambda^{\text{CO}})] \quad , \quad (1)$$

where the line emission  $I_\nu^{\text{line}}$  and gas-phase CO absorption  $\tau_\lambda^{\text{CO}}$  are obtained from a model,  $I_\nu^{\text{CD}}$  is the modeled aliphatic C–D emission feature discussed below, and  $I_\nu^{\text{cont}} \exp[-\tau_\lambda^{\text{dust}}]$  is the *observed* continuum (including PAH features, *except* for the aliphatic C–D feature  $I_\nu^{\text{CD}}$ ) interpolated over wavelengths where ice absorption is present.  $I_\nu^{\text{line}}$  includes emission from  $v = 1$  CO (Section 4.3). We

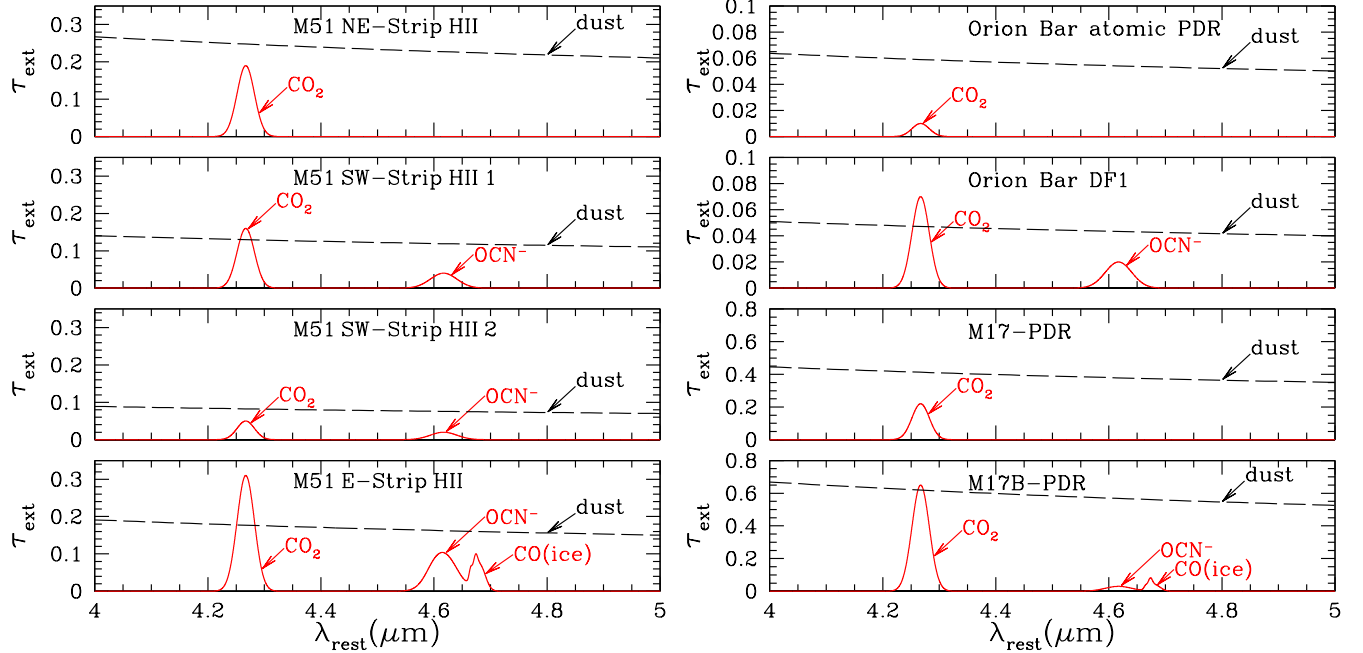


**Figure 3.** Estimated extinction due to dust (dashed curves) and ices (red curves) over the 4 – 5  $\mu\text{m}$  range for the four regions in M51 (see text).

assume that the hot  $v = 1$  CO is not at the same velocity as the bulk of the  $v = 0$  CO, so that they are not significantly absorbed by  $v = 0$  CO.

The H and He recombination lines are modeled using case B recombination calculations for H II (Storey & Hummer 1995) and He II (Del Zanna & Storey 2022). The He I 10833 Å triplet is assumed to be enhanced by a factor  $\sim 1.2$  due to radiative transfer effects (B.T. Draine et al. 2025, in preparation). For the four M51 H II regions we take the electron temperature  $T_e = 6000$  K (as determined for these regions by Croxall et al. 2015), and electron density  $n_e = 10^3 \text{ cm}^{-3}$ . For the ionized gas in the Orion Bar we take  $T_e = 9000$  K and  $n_e = 3000 \text{ cm}^{-3}$  (Pogge et al. 1992; Blagrove et al. 2007). For the ionized gas in M17 we take  $n_e = 500 \text{ cm}^{-3}$  and  $T_e \approx 8500$  K (García-Rojas et al. 2007).<sup>2</sup> For H I we include recombination lines from levels up to  $n = 49$ . Simple Gaussian line profiles are assumed for all lines, using the published  $R \equiv \lambda/\text{FWHM}$  for NIRSpec (Jakobsen et al. 2022).<sup>3</sup>

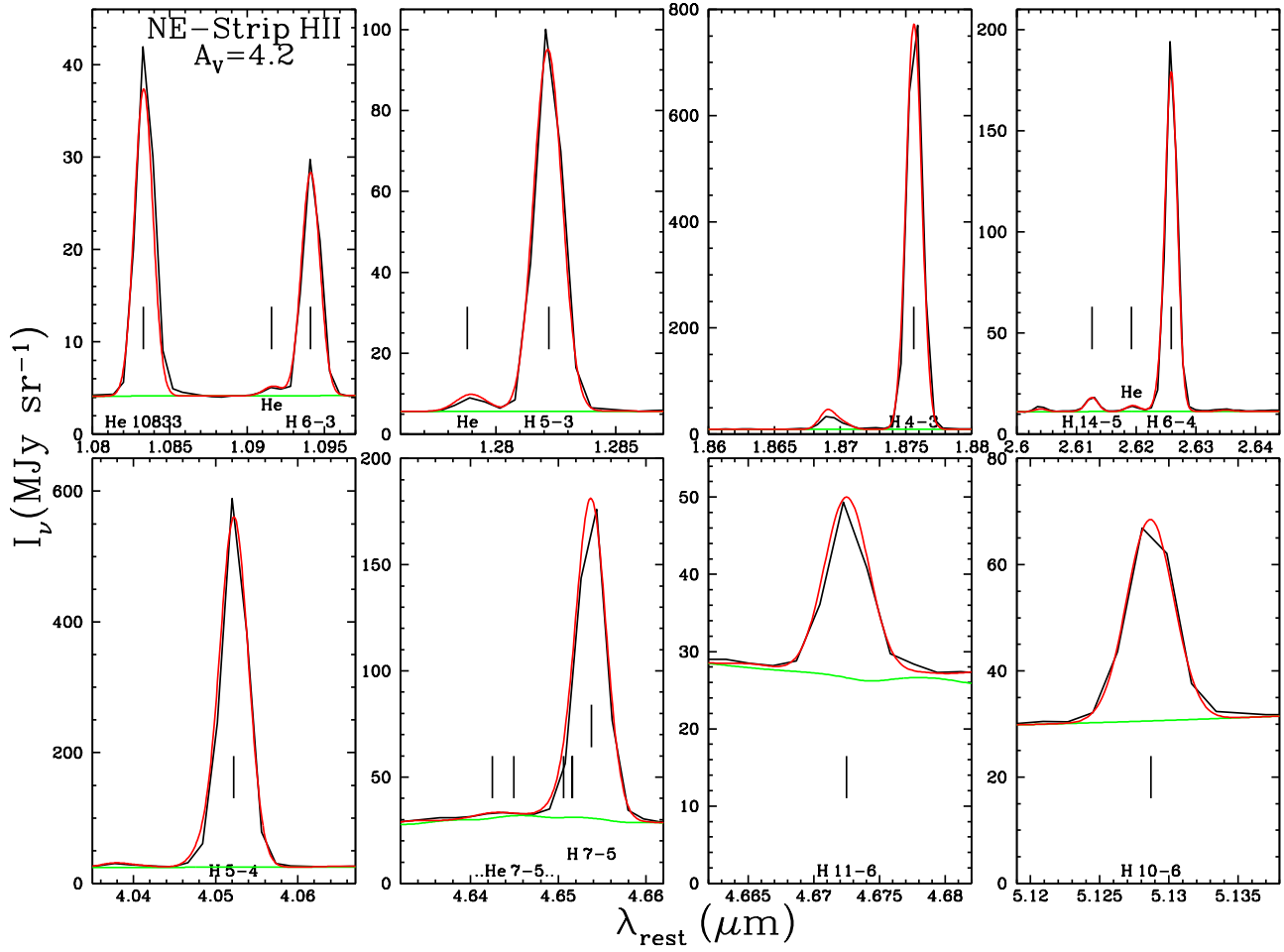
We fit emission measures  $\text{EM} \equiv \int n_e n(\text{H}^+) dL$  and He ionization  $\text{He}^+/\text{H}^+$  to reproduce the observed 1 – 5  $\mu\text{m}$  H and He recombination lines (including He I 1.0833  $\mu\text{m}$ , H Pa  $\gamma$  1.0941  $\mu\text{m}$ , H Pa  $\alpha$  1.876  $\mu\text{m}$ , and H Br  $\alpha$  4.052  $\mu\text{m}$ ) in each region. Reddening by dust (needed to reproduce the observed line ratios) is included, modeled as a uniform foreground screen, using the  $R_V = 5.5$  extinction curve from Gordon et al. (2023). Table 1 gives EM,  $\text{He}^+/\text{H}^+$ , and  $A_V$  for each region. Figure 3 shows the adopted  $\tau_{\text{dust}}(\lambda)$  for the four M51 regions in M51.

Figure 4 shows selected recombination lines for our most heavily-reddened M51 source, NE-Strip H II ( $A_V = 4.2$  mag). Agreement is excellent. The He I 7-5 emission near 4.65  $\mu\text{m}$  consists of a number of blended lines; the wavelengths of the strongest lines are shown. Similar results are found for the other three regions. Evidently, the adopted extinction law works well for 1 – 5  $\mu\text{m}$ .

#### 4.2. Ice Absorption

<sup>2</sup> For most of the H and He recombination lines, line ratios are insensitive to reasonable variations in  $n_e$  and  $T_e$ .

<sup>3</sup> Our M51 spectra and the M17 spectra were obtained with the NIRSpec medium resolution mode. The Orion Bar spectra (Peeters et al. 2024) were obtained with the high resolution mode.



**Figure 4.** Selected recombination lines for NE-Strip H II. Black curves: observed spectrum. Red curves: model = continuum (green) + line emission. The differential extinction between  $1.094\mu\text{m}$  ( $\text{Pa}\gamma$ ) and  $5.129\mu\text{m}$  ( $\text{Hu}\delta$ ) is consistent with the adopted [Gordon et al. \(2023\)](#)  $R_V = 5.5$  extinction curve and  $A_V = 4.2$  mag, with differential reddening  $A_{1.09} - A_{5.13} = 0.408A_V = 1.71$  mag determined to  $\pm 0.10$  mag.

Three of the four spectra in Figure 2 show strong absorption near  $4.26\mu\text{m}$  due to  $\text{CO}_2$  ice ([Gibb et al. 2004](#)), and the E-Strip H II spectrum has additional ice absorption features between  $\sim 4.55\mu\text{m}$  and  $\sim 4.70\mu\text{m}$  due to “XCN” (=  $\text{OCN}^-$ : [van Broekhuizen et al. 2004](#); [Öberg et al. 2011](#)) ice with a possible contribution from CO ice ([Gibb et al. 2004](#); [Onaka et al. 2022](#)). We determine  $\tau_{\text{ice}}(\lambda)$  by comparing the observed continuum with a smooth continuum interpolated between  $4.1$  and  $4.3\mu\text{m}$ , and between  $4.50$  and  $4.75\mu\text{m}$  (making allowance for the dust emission feature  $I_\nu^{\text{CD}}$  centered at  $4.65\mu\text{m}$ ). Our estimate for the optical depth of the  $\text{CO}_2$ ,  $\text{OCN}^-$ , and CO ice features is shown in Figure 3.

#### 4.3. Other Emission Lines

The  $4 - 5\mu\text{m}$  spectra also include emission lines from  $\text{H}_2$  and K III, which have been added to the model spectrum to reproduce the observed line strengths (see Table 1). For the Orion Bar positions we also add the O I multiplet at  $4.561\mu\text{m}$  reported by [Peeters et al. \(2024\)](#), presumed to be fluorescent emission. Our M51 spectra show no trace of this line.

Some of our M51 spectra show CO  $v = 1 \rightarrow 0$  emission lines, as previously seen in the Orion Bar ([Peeters et al. 2024](#)). Thus, our models include emission from  $v = 1$  CO, with rotational states ( $v = 1, J$ ) populated according to the rotational temperature  $T_{\text{rot,CO},v=1}$  given in Table 1. We use

Einstein  $A$  coefficients from [Chandra et al. \(1996\)](#). The CO emission is treated as optically thin; the lines are assumed to be sufficiently displaced in velocity to be unaffected by absorption by  $v = 0$  CO (see below).

#### 4.4. CO Absorption Lines

Some of our model spectra (Equation 1) include  $v = 0 \rightarrow 1$  absorption by CO, with the  $v = 0$  rotational levels assumed to be thermally populated with rotational excitation temperatures  $T_{\text{rot,CO},v=0}$  (see Table 1). The adopted CO column densities  $N(\text{CO}) \approx 10^{17} \text{ cm}^{-2}$  are consistent with  $n(\text{CO})/n(\text{H}_2) \approx 2 \times 10^{-4}$  in the molecular gas along the line of sight, as observed for cold molecular gas in the Galaxy ([Lacy et al. 2017](#)), although  $N(\text{CO})$  is not well constrained by the current data. See the Appendix for further details.

#### 4.5. Continuum and Dust Features

A smoothed continuum (emission from stars, dust, free-bound and free-free) was estimated for each of the regions, using the observed spectra between emission lines. The dust emission includes the well-known PAH emission features at  $3.29$  and  $3.4 \mu\text{m}$ , as well as weaker dust emission features and ice absorption features. The modeled emission and absorption lines are added to this continuum. As discussed below (Section 5.3), we find that we must add an emission feature near  $4.65 \mu\text{m}$  to reproduce the observed spectra.

#### 4.6. Uncertainties

In our model, all of the emission is assumed to be attenuated by a foreground screen with a single  $A_V$ , which is clearly unrealistic. Because the modeling also involves subjective decisions regarding (1) placement of continuum levels, (2) estimation of the strength and wavelength dependence of absorption by ices, and (3) choices regarding the central wavelength and FWHM of the  $4.65 \mu\text{m}$  feature, we do not attempt rigorous estimation of uncertainties. The uncertainties listed for different quantities in Table 1 are our subjective estimates; they are larger than would be estimated from statistical uncertainties alone.

### 5. RESULTS AND DISCUSSION

#### 5.1. The Selected Emission Regions

The areas in M51 selected here all include giant H II regions. From the hydrogen recombination lines, we infer the rate of hydrogen photoionizations,

$$\dot{N}_L = \alpha_B \text{EM} D^2 \Omega = 8.5 \times 10^{50} \left( \frac{\alpha_B}{3.8 \times 10^{-13} \text{ cm}^3 \text{ s}^{-1}} \right) \left( \frac{\text{EM}}{10^{23} \text{ cm}^{-5}} \right) \left( \frac{D}{7.5 \text{ Mpc}} \right)^2 \text{ s}^{-1} \quad (2)$$

for each region, where EM is the emission measure averaged over the extraction area with solid angle  $\Omega = 4.15 \times 10^{-11} \text{ sr}$ ,  $\alpha_B$  is the “case B” recombination rate coefficient ( $\alpha_B \approx 3.8 \times 10^{-13} \text{ cm}^3 \text{ s}^{-1}$  for  $T_e \approx 6000 \text{ K}$ ), and  $D = 7.5 \text{ Mpc}$  ([Csörnyei et al. 2023](#)) is the distance of M51. The inferred  $\dot{N}_L$  range from  $9 \times 10^{50} \text{ s}^{-1}$  for E-Strip H II to  $3.1 \times 10^{51} \text{ s}^{-1}$  for NE-Strip H II.

The  $\text{He}^+/\text{H}^+$  values of  $0.015 - 0.030$  inferred from the He I recombination lines (see Table 1) from the four regions in M51 correspond to ionization by stars of spectral type between O8.5V and O9V, with Lyman continuum photon emission rate  $Q_0 \approx 10^{48.1} \text{ s}^{-1}$  ([Martins et al. 2005](#)). Thus, each of the four regions contains  $\sim 10^3$  O stars (and many more B stars).

Molecular cloud material is abundant in each of these star-forming regions, given the  $\text{CO}_2$  ice absorption features in all four spectra (see Figure 2), strong  $\text{H}_2$  rovibrational emission lines, and evidence of gas-phase CO absorption and emission lines in some of the spectra (see below). Much of the stellar radiation is presumably reprocessed in photodissociation regions (PDRs) at the boundaries between H II regions and molecular clouds.



**Table 1.** Emission Parameters for Modeled Regions

	M51 NE-Strip <sup>a</sup>	M51 SW-Strip,1 <sup>b</sup>	M51 SW-Strip,2 <sup>b</sup>	M51 E-Strip <sup>c</sup>	Orion Atomic PDR	Orion DF1	M17 PDR	M17-B PDR
$v_r$ (km s <sup>-1</sup> ) <sup>d</sup>	420	500	485	500	18	18	25	15
$R_{gc}$ (kpc) <sup>e</sup>	4.13	4.25	4.34	1.12	8.2	8.2	6.5	6.5
$n_e$ (cm <sup>-3</sup> )	10 <sup>3</sup>	10 <sup>3</sup>	10 <sup>3</sup>	10 <sup>3</sup>	$3 \times 10^3$	$3 \times 10^3$	500	500
$T_e$ (K)	$6 \times 10^3$	$6 \times 10^3$	$6 \times 10^3$	$6 \times 10^3$	$9 \times 10^3$	$9 \times 10^3$	$8 \times 10^3$	$8 \times 10^3$
EM (10 <sup>23</sup> cm <sup>-5</sup> )	$3.65 \pm 0.1$	$1.90 \pm 0.1$	$1.00 \pm 0.1$	$2.05 \pm 0.10$	$60. \pm 5$	$30. \pm 3$	$14.5 \pm 1.0$	$120. \pm 10$
$\dot{N}_L$ (10 <sup>48</sup> s <sup>-1</sup> )	3100	1600	850	1700	—	—	—	—
He <sup>+</sup> /H <sup>+</sup>	$0.030 \pm 0.002$	$0.020 \pm 0.002$	$0.023 \pm 0.002$	$0.015 \pm 0.002$	$0.036 \pm 0.002$	$0.036 \pm 0.002$	$0.052 \pm 0.005$	$0.038 \pm 0.004$
$A_V$ (mag)	$4.2 \pm 0.2$	$2.2 \pm 0.2$	$1.4 \pm 0.2$	$3.0 \pm 0.2$	$1.0 \pm 0.2$	$0.8 \pm 0.2$	$7.0 \pm 0.5$	$10.5 \pm 0.5$
$N_{CO,v=0}$ (10 <sup>16</sup> cm <sup>-2</sup> )	10	1	0.5	30	0.3	0.5	10	10
$T_{rot,CO,v=0}$ (K)	15	15	15	40	15	15	15	15
$N_{CO,v=1}$ (10 <sup>6</sup> cm <sup>-2</sup> )	10	5	2	10	30	30	100	50
$T_{rot,CO,v=1}$ (K)	50	100	100	100	120	100	100	100
$F(\text{H}_2 4.4096\mu\text{m})^f$	$2.0 \pm 0.5$	$1.1 \pm 0.5$	$0.25 \pm 0.25$	$1.2 \pm 0.6$	$15 \pm 2$	$32 \pm 3$	$20 \pm 2$	$24 \pm 5$
$F(\text{H}_2 4.4171\mu\text{m})^f$	$1.5 \pm 0.5$	$0.7 \pm 0.5$	$0.2 \pm 0.2$	$0.7 \pm 0.6$	$12 \pm 2$	$20 \pm 3$	$16 \pm 2$	$20 \pm 4$
$F(\text{O I } 4.561\mu\text{m})^{f,h}$	$0.7 \pm 0.7$	$< 0.3$	$< 0.2$	$< 0.3$	$50 \pm 5$	$4 \pm 1$	$4 \pm 4$	$12 \pm 4$
$F(\text{H}_2 4.5757\mu\text{m})^f$	$0.4 \pm 0.4$	$0.2 \pm 0.2$	$< 1$	$0.4 \pm 0.3$	$3 \pm 2$	$10 \pm 2$	$4 \pm 4$	$9 \pm 2$
$F([\text{K III}] 4.6180\mu\text{m})^f$	$11.5 \pm 1.0$	$4.5 \pm 0.5$	$1.6 \pm 0.2$	$1.1 \pm 0.1$	$95 \pm 10$	$53 \pm 5$	$45 \pm 5$	$430 \pm 40$
$F(\text{H}_2 4.6947\mu\text{m})^f$	$7.0 \pm 0.7$	$4.3 \pm 0.5$	$1.5 \pm 0.3$	$6.0 \pm 0.5$	$65 \pm 6$	$155 \pm 10$	$90 \pm 5$	$110 \pm 10$
$B_{\text{aliph.CD}}$ (MJy sr <sup>-1</sup> ) <sup>g</sup>	$8.5 \pm 0.8$	$6.5 \pm 1.0$	$2.7 \pm 0.7$	$5.0 \pm 1.3$	$75 \pm 11$	$55 \pm 8$	$45 \pm 9$	$90 \pm 18$
$B_{4.35\mu\text{m}}$ (MJy sr <sup>-1</sup> ) <sup>g</sup>	$< 1.0$	$< 0.7$	$< 0.5$	$< 1.0$	$< 20$	$< 10$	$< 10$	$< 10$
$B_{4.40\mu\text{m}}$ (MJy sr <sup>-1</sup> ) <sup>g</sup>	$< 1.0$	$< 0.5$	$< 0.5$	$< 1.0$	$< 10$	$< 10$	$< 8$	$< 10$
$B_{4.75\mu\text{m}}$ (MJy sr <sup>-1</sup> ) <sup>g</sup>	$< 1.0$	$< 1.0$	$< 0.5$	$< 1.5$	$< 15$	$< 15$	$< 8$	$< 20$
$F_{\text{aliph.CD}}(4.65\mu\text{m})$	$38. \pm 4$	$32. \pm 5$	$14. \pm 4$	$23. \pm 6$	$410. \pm 60$	$300. \pm 45$	$175. \pm 35$	$280. \pm 60$
$F_{\text{arom.CD}}(4.40\mu\text{m})$	$< 18$	$< 8$	$< 8$	$< 17$	$< 150$	$< 150$	$< 200$	$< 200$
$F_{\text{arom.CD}}(4.75\mu\text{m})$	$< 8$	$< 9$	$< 5$	$< 13$	$< 140$	$< 140$	$< 55$	$< 110$
$F_{\text{arom.CH}}^{\text{clip,corr}}(3.29\mu\text{m})^{f,g}$	$1610 \pm 80$	$915 \pm 50$	$376 \pm 20$	$925 \pm 50$	$36500 \pm 1100$	$23300 \pm 700$	$8780 \pm 440$	$13300 \pm 670$
$F_{\text{nonarom.CH}}^{\text{clip,corr}}(3.4\mu\text{m})^{f,g}$	$395 \pm 40$	$225 \pm 23$	$87 \pm 9$	$212 \pm 21$	$7380 \pm 370$	$5140 \pm 260$	$2500 \pm 250$	$3860 \pm 390$
$F_{\text{aliph.CD}}^{\text{corr}}(4.65\mu\text{m})^{f,g}$	$49 \pm 5$	$38 \pm 6$	$16 \pm 4$	$43 \pm 7$	$434 \pm 65$	$318 \pm 48$	$260 \pm 50$	$520 \pm 100$
$F_{\text{arom.CD}}^{\text{corr}}(4.40\mu\text{m})^{f,g}$	$< 14$	$< 7$	$< 7$	$< 14$	$< 140$	$< 140$	$< 110$	$< 140$
$F_{\text{nitrileCN}}^{\text{corr}}(4.35\mu\text{m})^{f,g,i}$	$< 15$	$< 10$	$< 7$	$< 15$	$< 300$	$< 150$	$< 150$	$< 150$
$F_{\text{arom.CD}}^{\text{corr}}(4.75\mu\text{m})^{f,g,j}$	$< 10$	$< 10$	$< 5$	$< 15$	$< 150$	$< 150$	$< 80$	$< 200$
$F_{\text{nonarom.CH}}^{\text{clip,corr}}/F_{\text{arom.CH}}^{\text{clip,corr}}$	0.246	0.246	0.232	0.229	0.202	0.221	0.284	0.290
$F_{\text{aliph.CD}}^{\text{corr}}/F_{\text{nonarom.CH}}^{\text{clip,corr}}$	0.12	0.17	0.18	0.14	0.059	0.062	0.10	0.13
$F_{\text{arom.CD}}^{\text{corr}}/F_{\text{arom.CH}}^{\text{clip,corr}}$	$< 0.009$	$< 0.008$	$< 0.019$	$< 0.015$	$< 0.004$	$< 0.006$	$< 0.013$	$< 0.010$
$F_{\text{nitrileCN}}^{\text{corr}}/F_{\text{arom.CH}}^{\text{clip,corr}}$	$< 0.009$	$< 0.011$	$< 0.019$	$< 0.015$	$< 0.008$	$< 0.006$	$< 0.016$	$< 0.011$
$F_{4.75\mu\text{m}}^{\text{corr}}/F_{\text{arom.CH}}^{\text{clip,corr}}$	$< 0.006$	$< 0.011$	$< 0.013$	$< 0.016$	$< 0.004$	$< 0.006$	$< 0.009$	$< 0.015$

<sup>a</sup> NE-Strip H II = NGC5194+91.0+69.0 (Croxall et al. 2015)<sup>b</sup> SW-Strip H II-1 and H II-2 = NGC 5194-86.5-79.4 (Croxall et al. 2015)<sup>c</sup> E-Strip H II = NGC5194+30.2+2.2 (Croxall et al. 2015)<sup>d</sup> Heliocentric radial velocity.<sup>e</sup> Distance from galaxy center.<sup>f</sup> Surface brightness of line or feature (10<sup>-6</sup> erg cm<sup>-2</sup> s<sup>-1</sup> sr<sup>-1</sup>)<sup>g</sup> Extinction-corrected.<sup>h</sup> O I  $2p^34p \rightarrow 2p^33d \rightarrow 3D_{J'}$ .<sup>i</sup> Assuming FWHM  $\lesssim 0.06\mu\text{m}$ .<sup>j</sup> Assuming FWHM =  $0.047\mu\text{m}$  (Doney et al. 2016).

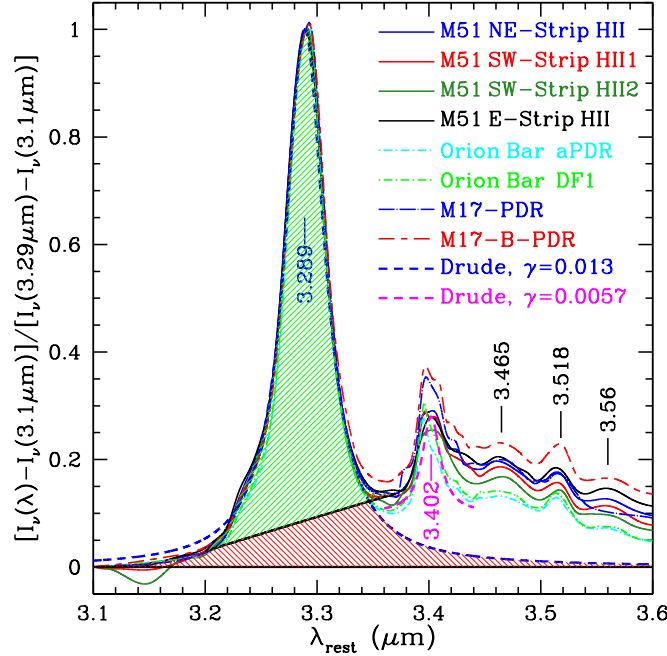


**Figure 5.** Comparison of the 3.1 – 3.65  $\mu\text{m}$  emission in the different regions. The 3.29  $\mu\text{m}$  feature profile is nearly invariant. The 3.37 to 3.60  $\mu\text{m}$  emission shows regional variations in strength (relative to the 3.29  $\mu\text{m}$  feature), and in spectral details (see text). Dashed curves: Drude profiles for the 3.29 and 3.40  $\mu\text{m}$  components (see text). The green shaded area shows the power included in  $F_{\text{arom.CH}}^{\text{clip}}$ ; the red shaded area shows the power in the Drude profile that is missed in  $F_{\text{arom.CH}}^{\text{clip}}$ . We find  $F_{\text{arom.CH}}^{\text{clip}}/F_{\text{arom.CH}} \approx 0.71$ .

### 5.2. The C–H Stretch Emission Features

Figure 5 shows normalized 3.1 – 3.65  $\mu\text{m}$  emission spectra (after removal of emission lines by interpolation) from the four H II region extractions in M51, the two Orion Bar positions, and the two positions in M17. In addition to the strong peak at 3.29  $\mu\text{m}$ , all eight spectra exhibit a broad feature extending from 3.37 to 3.60  $\mu\text{m}$ . This complex appears equivalent to the broad “plateau” at 3.47  $\mu\text{m}$  found at lower resolution by Lai et al. (2020), resolved at higher resolution into peaks at 3.402, 3.465, 3.518, and 3.56  $\mu\text{m}$ .

The 3.29  $\mu\text{m}$  feature is the aromatic C–H stretching mode in polycyclic aromatic hydrocarbons (Leger & Puget 1984; Allamandola et al. 1985; Tielens 2008). The similarity of the 3.29  $\mu\text{m}$  feature in the eight spectra is striking. Except for the wings, the 3.29  $\mu\text{m}$  feature can be approximated by a Drude profile

$$I_{\nu}^{\text{CD}} = B \frac{\gamma^2}{(\lambda/\lambda_0 - \lambda_0/\lambda)^2 + \gamma^2} \quad (3)$$

with central wavelength  $\lambda_{\text{arom.CH}} = 3.289 \mu\text{m}$  and FWHM = 0.0423  $\mu\text{m}$  ( $\gamma_{\text{arom.CH}} = 0.013$ ), as shown in Figure 5.

The broad emission feature extending from 3.37 – 3.60  $\mu\text{m}$  presumably includes a small contribution from aromatic C–H overtone emission (Allamandola et al. 1989), but is dominated by C–H stretching modes in nonaromatic material. The 3.40  $\mu\text{m}$  feature [which Peeters et al. (2024) find to be composed of sub-components centered at 3.395, 3.403, and 3.424  $\mu\text{m}$ ] is generally ascribed to the C–H stretch in methylene ( $-\text{CH}_2-$ ) groups in aliphatic hydrocarbons (Allamandola et al. 1989). The 3.46  $\mu\text{m}$  and

$3.52\mu\text{m}$  emission features have been attributed to H attached to diamondlike carbon (Allamandola et al. 1992; Van Kerckhoven et al. 2002).

Let  $F_{\text{arom.CH}}$  be the power in the  $3.29\mu\text{m}$  aromatic C–H stretch feature and  $F_{\text{nonarom.CH}}$  be the power in the  $3.37–3.60\mu\text{m}$  nonaromatic C–H stretch features. Decomposition of the observed emission into components plus an underlying continuum is problematic because of both blending and the uncertain nature of the underlying emission “plateau”.<sup>4</sup>

We quantify  $F_{\text{arom.CH}}$  and  $F_{\text{nonarom.CH}}$  using the model-free empirical “clipping” method<sup>5</sup> described in Draine et al. (2021). Figure 6 shows two examples of this clipping procedure; the shaded areas show the integrated power included in  $F_{\text{arom.CH}}^{\text{clip}}$  and  $F_{\text{nonarom.CH}}^{\text{clip}}$ . Correcting for extinction,

$$F_{\text{arom.CH}}^{\text{clip,corr}} = e^{\tau_{3.29}} F_{\text{arom.CH}}^{\text{clip}} \quad (4)$$

$$F_{\text{nonarom.CH}}^{\text{clip,corr}} = e^{\tau_{3.40}} F_{\text{nonarom.CH}}^{\text{clip}} \quad (5)$$

where  $\tau_{3.29}$  and  $\tau_{3.40}$  are obtained from the Gordon et al. (2023) extinction curve with  $A_V$  determined from the H I recombination lines. Define

$$f \equiv \frac{F_{\text{aliph.CH}}}{F_{\text{nonarom.CH}}^{\text{clip}}} \quad (6)$$

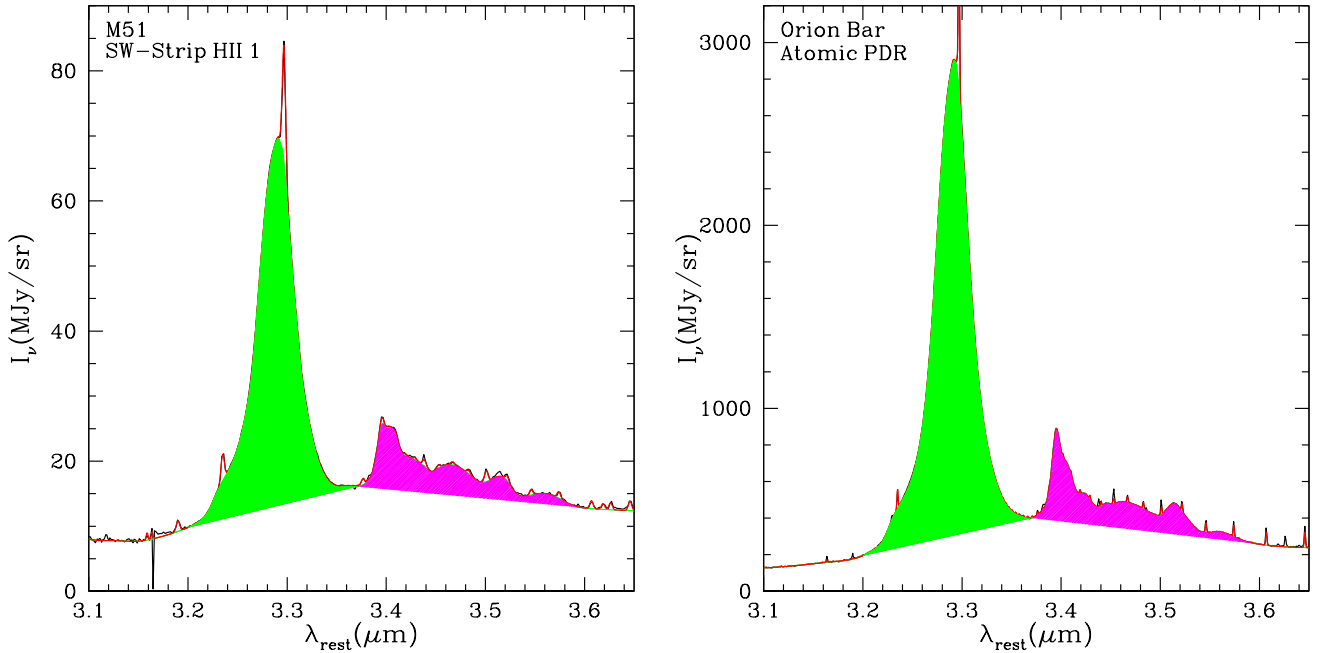


**Figure 6.** The  $3–4\mu\text{m}$  spectra of SW-Strip H II in M51 (left) and the “atomic PDR” in the Orion Bar (right). Red curve: model spectrum including emission lines. Areas shaded green and magenta show how the integrated intensities  $F_{\text{arom.CH}}^{\text{clip}}$  and  $F_{\text{nonarom.CH}}^{\text{clip}}$  are evaluated (see text).

<sup>4</sup> See, e.g., the alternative decompositions shown in Figure 16 of Peeters et al. (2024).

<sup>5</sup>  $\lambda F_\lambda^{\text{cut}} = a \ln \lambda + b$  is defined passing through  $\lambda F_\lambda^{\text{obs}}$  at “clip points”  $\lambda_1, \lambda_2 = 3.20, 3.37\mu\text{m}$  for the aromatic feature, and  $3.37, 3.60\mu\text{m}$  for the nonaromatic feature. The power in each feature is  $F^{\text{clip}} = \int_{\lambda_1}^{\lambda_2} (F_\lambda^{\text{obs}} - F_\lambda^{\text{cut}}) d\lambda$ .

**Table 2.** Comparison with Previous Work

Feature	Region	This Work <sup>a</sup> ( $10^{-6} \text{ erg cm}^{-2} \text{ s}^{-1} \text{ sr}^{-1}$ )	Previous Work ( $10^{-6} \text{ erg cm}^{-2} \text{ s}^{-1} \text{ sr}^{-1}$ )	Reference
Aliphatic CD	Orion Bar, atomic PDR	$410 \pm 60$	350	(Peeters et al. 2024)
”	Orion Bar, DF1	$300 \pm 45$	220	(Peeters et al. 2024)
”	M17-B-PDR	$280 \pm 60$	$273 \pm 52$	(Boersma et al. 2023)
4.75 $\mu\text{m}$ feature	Orion Bar, atomic PDR	$< 140$	50	(Peeters et al. 2024)
”	Orion Bar, DF1	$< 140$	90	(Peeters et al. 2024)

<sup>a</sup> Not corrected for reddening.

to be the ratio of the true aliphatic C–H emission to the “clipped” measure of the nonaromatic C–H emission. Blending and uncertainties about the level of the emission underlying the nonaromatic features make it difficult to determine  $f$ ; we take  $f \approx 1.0$  as a working estimate.

### 5.3. Emission from Aliphatic C–D

Figure 7 shows 4.5 – 4.8 $\mu\text{m}$  spectra for the four regions in M51; Figure 8 shows the same spectral region for two positions in the Orion Bar (Peeters et al. 2024) and two positions in the M17 PDR (Boersma et al. 2023). As evident in Figure 2, the M51 spectra include a significant dust emission feature centered near 4.65 $\mu\text{m}$ , near the expected wavelength of the aliphatic C–D stretch, similar to the 4.65 $\mu\text{m}$  feature found in M17 by Boersma et al. (2023) and in the Orion Bar by Peeters et al. (2024).

To fit this feature, for all regions we adopt a simple Drude profile (Equation (3)) with central wavelength  $\lambda_{\text{aliph.CD}} = 4.647\mu\text{m}$  and FWHM = 0.0265 $\mu\text{m}$  ( $\gamma_{\text{aliph.CD}} = 0.0057$ ). The peak intensity  $B_{\text{aliph.CD}}$  is adjusted so that Equation (1) approximates the observed emission for each region, as shown in Figures 7 and 8. There is no reason to expect the actual emission profile to conform to Equation (3), but with the signal-to-noise ratio of the present spectra, in a region crowded with numerous emission lines, our Drude profile provides an acceptable fit. Future observations may permit refinement of the aliphatic C–D emission profile.

For the Drude profile, the extinction-corrected integrated intensity

$$F_{\text{aliph.CD}}^{\text{corr}} = \int I_{\nu}^{\text{CD}} d\nu = \frac{\pi c}{2} \frac{\gamma_{\text{aliph.CD}} B_{\text{aliph.CD}}}{\lambda_{\text{aliph.CD}}} \quad (7)$$

for each region is given in Table 1.

The aliphatic C–D stretch was previously detected in M17-B-PDR (Boersma et al. 2023) and in the Orion Bar atomic PDR and DF1 (Peeters et al. 2024). Table 2 compares those results with our estimates for these features. We also compare our upper limit for the 4.75 $\mu\text{m}$  feature in the Orion Bar with the feature intensity measured by Peeters et al. (2024).

### 5.4. Regional Variations in Deuteration

The strength of the 4.65 $\mu\text{m}$  aliphatic C–D emission relative to the 3.37 – 3.60 $\mu\text{m}$  nonaromatic C–H emission varies significantly among the four regions in M51 – see Figure 9a, which plots  $F(4.65\mu\text{m})/F(3.4\mu\text{m})$  for the four regions in M51, and also for two positions in the Orion Bar, and two positions in the M17 PDR. What is responsible for the variations in  $F(4.65\mu\text{m})/F(3.4\mu\text{m})$ ?

Previous studies have shown that the aliphatic/aromatic ratio shows regional variations in the Milky Way and other galaxies (Lai et al. 2020; Yang & Li 2023b). However, in Figure 9a there is no apparent correlation of  $F(4.65\mu\text{m})/F(3.4\mu\text{m})$  with  $F(3.4\mu\text{m})/F(3.29\mu\text{m})$ . Evidently, the environmental effects

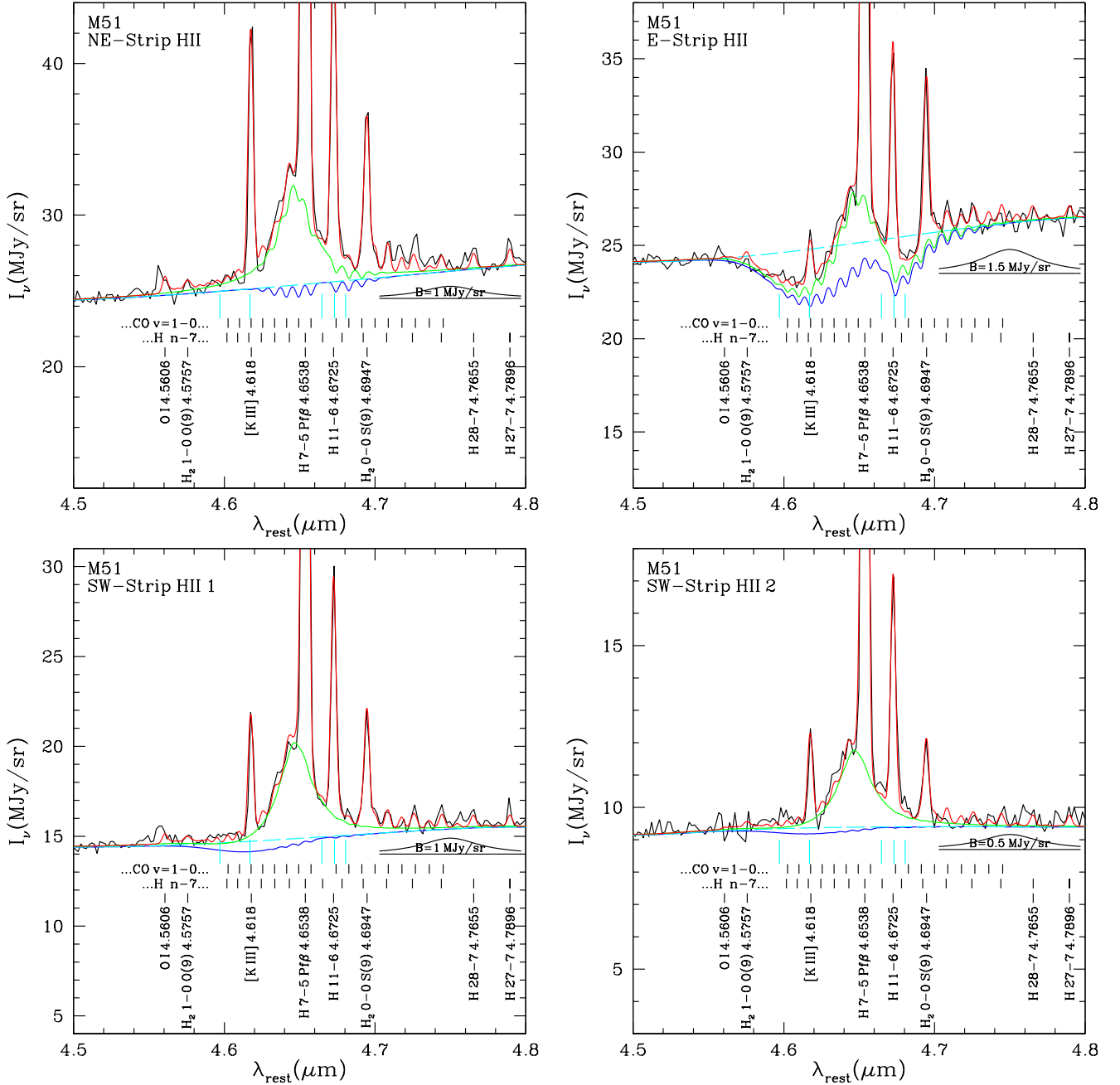


**Figure 7.** The 4.5 – 4.8  $\mu\text{m}$  spectra of the four sightlines in Figure 2. Black curves: observed spectra. Dashed cyan curves: estimate for the dust-attenuated “continuum” (not including 4.65  $\mu\text{m}$  feature), but without absorption by ice or CO. Solid blue curves: continuum after absorption by ice and  $v = 0$  CO. Green curves: continuum plus 4.65  $\mu\text{m}$  emission feature (Eq. 3) with attenuation by dust, ice, and CO. Red curves: green curves plus emission lines of H, He,  $\text{H}_2$ ,  $v = 1$  CO, and [K III] (see text). Inset profile: upper limit on an emission feature at 4.75  $\mu\text{m}$  (see text).

responsible for the variations in the aromatic/nonaromatic ratio do not directly lead to variations in deuteration.

Another quantity that varies from region to region is  $\text{He}^+/\text{H}^+$ , measuring the degree of helium ionization in associated H II regions. Figure 9(b) plots  $F(4.65\mu\text{m})/F(3.4\mu\text{m})$  versus  $\text{He}^+/\text{H}^+$ . At



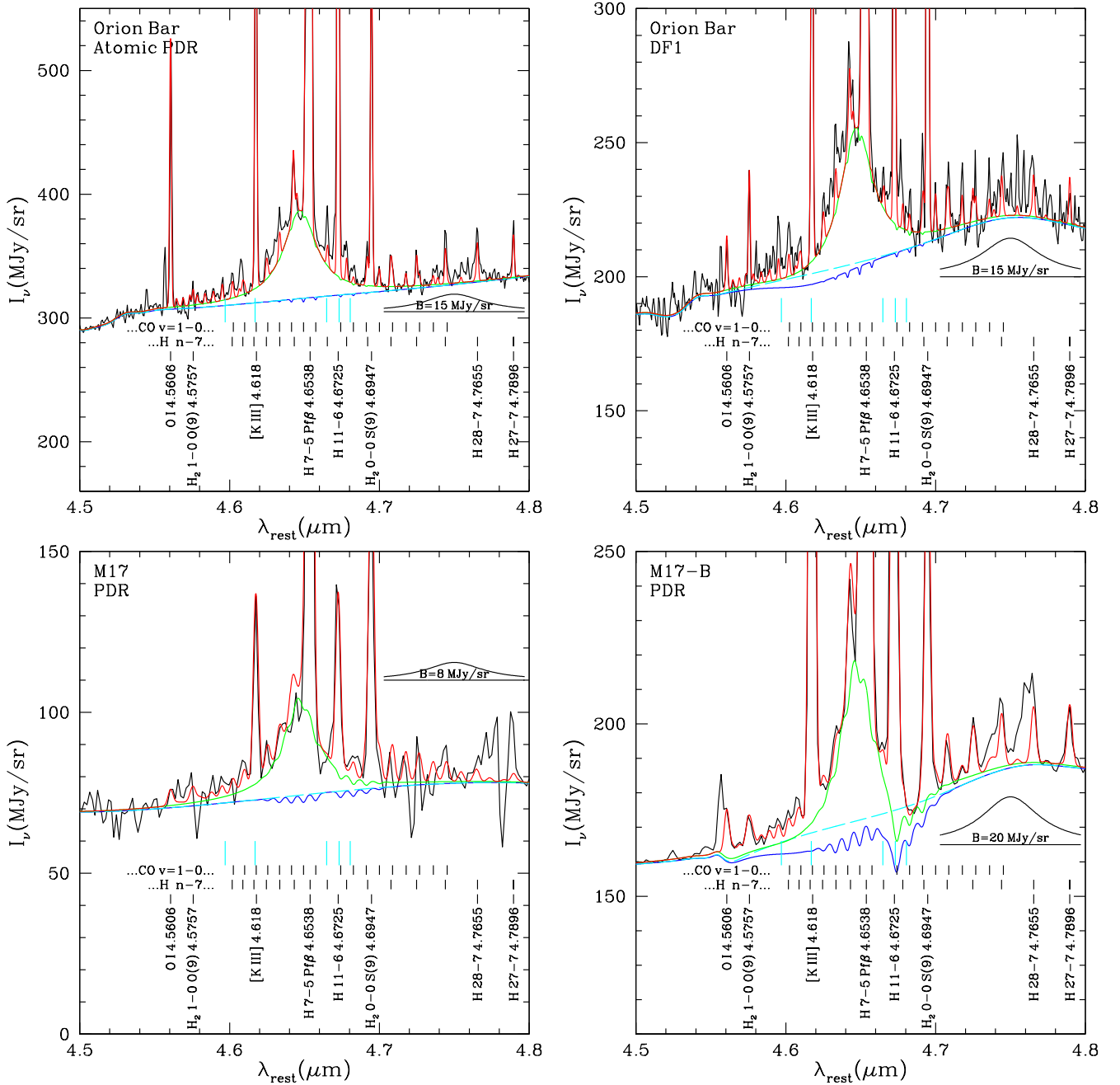


**Figure 8.** Same as Figure 7, but for two pointings in the Orion Bar (Peeters et al. 2024), and two positions in the M17 PDR (Boersma et al. 2023) (see text).

least in this sample,  $F(4.65\mu\text{m})/F(3.4\mu\text{m})$  shows a negative correlation with  $\text{He}^+/\text{H}^+$ . Possible explanations for this trend are discussed below in Section 5.6.

### 5.5. The D/H Ratio in the Nanoparticles

The integrated absorption cross section (“band strength”)  $A \equiv \int \sigma_\nu d\lambda^{-1}$  per C–D or C–H bond is expected to be smaller for C–D (relative to C–H) by about a factor  $A_{\text{CH}}/A_{\text{CD}} \approx 1.75$  (Bauschlicher

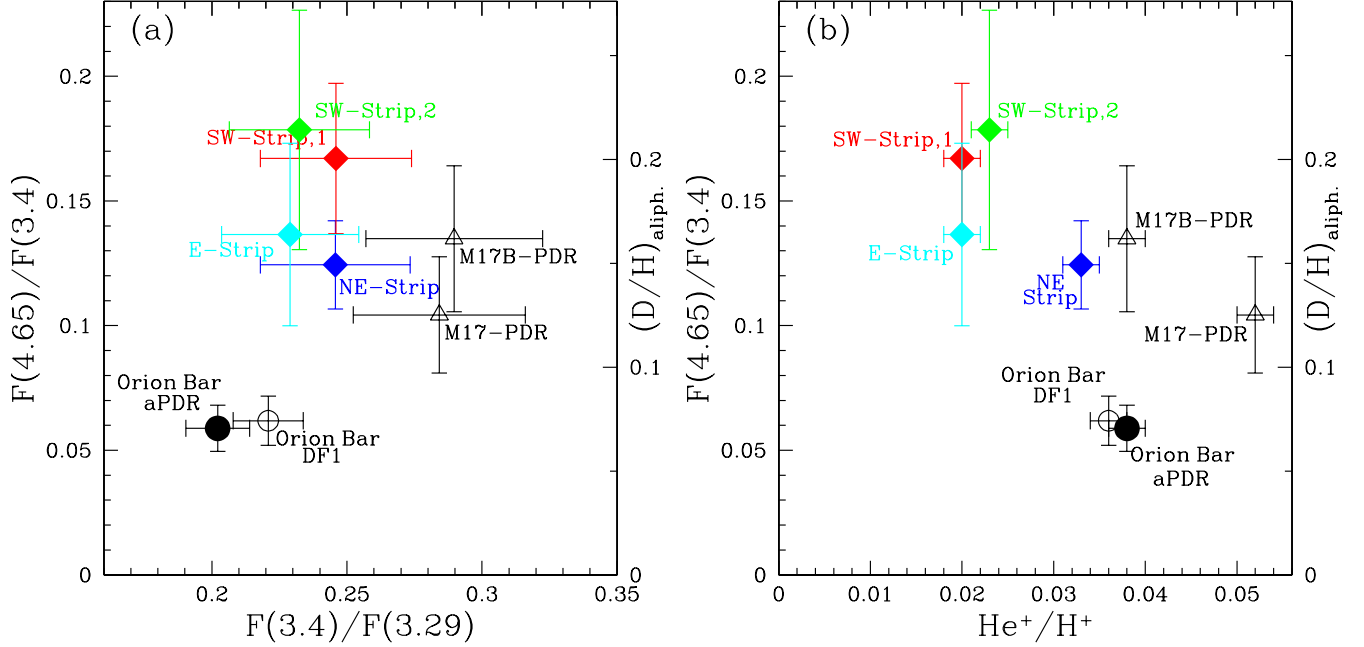


**Figure 9.** (a)  $F(4.65)/F(3.4)$  vs.  $F(3.4)/F(3.29)$ , where  $F(4.65)$  is the power in the  $4.65\mu\text{m}$  aliphatic C-D feature,  $F(3.4)$  is the “clipped” estimate of the non-aromatic C-H stretch power, and  $F(3.29)$  is the “clipped” estimate of the aromatic C-H stretch power (see Figure 6). The right-hand scale shows the estimated  $(D/H)_{\text{aliph.}}$  in the emitting nanoparticles, assuming  $K/f = 1.2$ . Deuteration is 2-3 times higher in M51 than in the Orion Bar.  $(D/H)_{\text{aliph.}}$  does not appear to be correlated with nonaromatic fraction. (b) Same as (a), but plotted against  $\text{He}^+/\text{H}^+$ .  $(D/H)_{\text{aliph.}}$  appears to depend on the hardness of the radiation ionizing the H II region associated with the PDR where the PAHs are located.

et al. 1997).<sup>6</sup> The D/H ratio of the aliphatic material in the emitting nanoparticles is related to the observed emission by

$$\left(\frac{D}{H}\right)_{\text{aliph.}} = K \times \frac{F_{\text{aliph. CD}}^{\text{corr}}}{F_{\text{aliph. CH}}^{\text{corr}}} = \frac{K}{f} \times \frac{F_{\text{aliph. CD}}^{\text{corr}}}{F_{\text{nonarom. CH}}^{\text{clip, corr}}}, \quad (8)$$

where  $f \approx 1$  is the factor relating the aliphatic C-H emission to  $F_{\text{nonarom. CH}}^{\text{clip, corr}}$  (Equation 6), and

$$K = 1.75 \left(\frac{\lambda_{\text{CD}}}{\lambda_{\text{CH}}}\right)^3 \left(\frac{\int [e^{hc/\lambda_{\text{CH}} k_B T} - 1]^{-1} (dP/dT) dT}{\int [e^{hc/\lambda_{\text{CD}} k_B T} - 1]^{-1} (dP/dT) dT}\right). \quad (9)$$

Here  $dP/dT$  is the temperature distribution function for the nanoparticles responsible for the  $\lambda < 5\mu\text{m}$  emission. Estimation of D/H requires knowledge of the temperature distribution function  $dP/dT$ , requiring modeling of the stochastic heating process (Draine & Li 2001), which depends on the particle size. However, if we assume that the emitting material can be characterized by a temperature in  $500\text{ K} < T < 1500\text{ K}$ , then we find  $0.5 < K < 1.9$ , i.e.,

$$K \approx 1.2 \pm 0.7, \quad (10)$$

<sup>6</sup> Mori et al. (2022) find  $A_{\text{CH}}/A_{\text{CD}} = 2.6$  for the aliphatic bonds. This would raise the inferred D/H ratio by a factor  $\sim 1.5$ .

**Table 3.** Deuteration in Modeled Regions

region	(D/H) <sub>aliphatic</sub> <sup>a</sup>	(D/H) <sub>aromatic</sub> <sup>b</sup>
M51: NE-Strip	0.15 ± 0.02	< 0.007
M51: SW-Strip,1	0.20 ± 0.04	< 0.006
M51: SW-Strip,2	0.21 ± 0.06	< 0.016
M51: E-Strip	0.17 ± 0.04	< 0.013
Orion Bar: atomic PDR	0.071 ± 0.011	< 0.003
Orion Bar: DF1	0.074 ± 0.012	< 0.005
M17-PDR	0.125 ± 0.028	< 0.022
M17-B-PDR	0.16 ± 0.04	< 0.018

<sup>a</sup> Assuming  $K = 1.2$  and  $F_{\text{aliph.CH}}/F_{\text{nonarom.CH}}^{\text{clip}} = 1$  (see text).

<sup>b</sup> Assuming  $K = 1.2$  and  $F_{\text{arom.CH}}/F_{\text{arom.CH}}^{\text{clip}} = 1/0.71$  (see text).

with  $K = 1.2$  corresponding to an emitting temperature  $T = 900$  K. In the discussion below, we take  $K = 1.2$  and  $f = 1$ .

Results for  $(\text{D}/\text{H})_{\text{aliph.}}$  are given in Table 3, and on the right-hand scale in Figure 9b. The four positions in M51 show  $(\text{D}/\text{H})_{\text{aliph}}$  varying by a factor of  $\sim 1.3$ , from 0.15 in NE-Strip to 0.21 in SW-Strip,2. The four positions in M51 have

$$\langle \text{D}/\text{H} \rangle_{\text{aliph}} \approx 0.17 \pm 0.02 \quad . \quad (11)$$

For the Orion Bar positions we find  $\langle \text{D}/\text{H} \rangle_{\text{aliph}} = 0.07 \pm 0.01$ , smaller than the values 0.23 and 0.16 found by Peeters et al. (2024). For M17 we find  $\langle \text{D}/\text{H} \rangle_{\text{aliph}} = 0.14 \pm 0.02$ , smaller than the value  $0.31 \pm 0.13$  found by Boersma et al. (2023), and intermediate between the Orion Bar and the four regions in M51.

The aliphatic material in M51 is D-enriched by a factor  $\sim 10^4$  relative to the overall abundance  $\text{D}/\text{H} \approx 23$  ppm. It must be stressed that  $(\text{D}/\text{H})_{\text{aliph.}}$  is only determined for the nanoparticles small enough ( $N_{\text{C}} \lesssim 10^3$  C atoms) that single-photon heating (with  $h\nu < 13.6$  eV) can heat them to the high temperatures ( $T \gtrsim 500$  K) required to radiate effectively at  $4.6\mu\text{m}$ . The majority of the hydrocarbon material is in larger particles, which may have a different D/H ratio but are unconstrained by  $\lambda < 5\mu\text{m}$  emission spectra.

The  $4.65\mu\text{m}$  feature is narrow, with a fractional width  $\gamma_{\text{CD}} \equiv \text{FWHM}/\lambda_{\text{CD}} \approx 0.006$  – similar to the fractional width of the  $3.40\mu\text{m}$  aliphatic component of the nonaromatic C–H emission extending from  $3.36 - 3.60\mu\text{m}$  (see Figure 5).

### 5.6. Possible Interpretation of the $(\text{D}/\text{H})_{\text{aliph.}} - \text{He}^+/\text{H}^+$ Anticorrelation

Figure 9(b) shows that the highest degree of deuteration is seen for the regions with the lowest values of  $\text{He}^+/\text{H}^+$ . The PAH emission in star-forming regions originates primarily in PDRs adjacent to H II regions. As the stellar population ages, the intensity of the  $h\nu < 13.6$  eV radiation powering the PDRs declines, and the far-UV spectrum softens (Smith et al. 2002).

One possible interpretation for the anticorrelation of aliphatic deuteration and  $\text{He}^+/\text{H}^+$  is that the  $h\nu < 13.6$  eV radiation in the PDRs is harsher – both more intense, and with a harder spectrum – in regions with younger stars, as measured by  $\text{He}^+/\text{H}^+$ . In the quiescent ISM, single-photon heating events that lead to H loss from small PAHs are relatively rare, and the small difference in binding energy may lead to strong preferential retention of D, leading to the observed high levels of deuteration. However, in a high intensity PDR with a hard FUV spectrum, the combination of more frequent “multiphoton” heating events (where a photoabsorption occurs before the PAH has fully cooled following the previous photoabsorption) and harder FUV photons may lead to rapid

loss of both D and H, and a drop in the degree of deuteration as the more abundant H atoms from the gas replace the losses. If the hydrocarbon nanoparticles are deuterated prior to the arrival of the photodissociation front and then lose deuterium in the PDR, perhaps they lose deuterium more rapidly in the harsher PDRs near the youngest stellar clusters.

Because loss of deuterium begins as soon as the nanoparticles are exposed to FUV in the PDR, the particles responsible for emission in the  $4.65\mu\text{m}$  C-D and  $3.42\mu\text{m}$  C-H features have already undergone partial D loss – the D/H ratio in the not-yet-exposed nanoparticles should be higher than the value estimated from the observed emission.

### 5.7. Upper Limits on Aromatic C-D

The aromatic C-D stretch is expected to be located at  $\lambda_{\text{arom.CD}} \approx 4.40\mu\text{m}$  (Boersma et al. 2023, V. J. Esposito 2024, private communication). As discussed in Section 5.2, the  $3.29\mu\text{m}$  aromatic C-H stretch can be approximated by a Drude profile (Equation (3)) with  $\gamma_{\text{arom.CH}} = 0.013$ . The aromatic C-D stretch resulting from substitution of D for H might be expected to have similar dimensionless width  $\gamma_{\text{arom.CD}} \approx 0.013$  (FWHM  $\approx 0.057\mu\text{m}$ ).

An emission feature near  $4.40\mu\text{m}$  was tentatively detected in ISO spectra of the Orion Bar (Peeters et al. 2004), and appeared to be present in  $R \approx 100$  AKARI spectra of a massive young stellar object (Onaka et al. 2022), with FWHM  $\approx 0.045\mu\text{m}$ . However, Boersma et al. (2023) found no evidence for an emission feature near  $4.40\mu\text{m}$  in JWST spectra of a number of PDRs, and JWST spectra of the Orion Bar do not show a feature at  $4.40\mu\text{m}$ , instead showing a broad feature near  $4.35\mu\text{m}$  with FWHM  $\approx 0.1\mu\text{m}$ , which was suggested to be a combination of the nitrile C-N stretch and the aromatic C-D stretch (Allamandola et al. 2021; Peeters et al. 2024; Esposito et al. 2024).

Figure 10 shows  $4.2 - 4.6\mu\text{m}$  spectra for the four regions in M51. There is no evidence of an emission feature centered near the expected wavelength  $4.40\mu\text{m}$  in any of the M51 spectra. Each panel of Figure 10 includes a sample profile with  $\lambda_{\text{arom.CD}} = 4.40\mu\text{m}$ ,  $\gamma_{\text{arom.CD}} = 0.013$ , and an amplitude  $B_{\text{arom.CD}}^{\text{up.lim.}}$  that would have made the feature discernible in the observed spectrum (unless the underlying continuum conspired to have a local minimum with similar central wavelength and width). We take the amplitude of these illustrative features to be an upper limit on the power,

$$F_{\text{arom.CD}}^{\text{corr}} = \frac{\pi C}{2} \frac{\gamma_{\text{arom.CD}}}{\lambda_{\text{arom.CD}}} \times B_{\text{arom.CD}} \quad , \quad (12)$$

in the aromatic C-D stretch feature. Upper limits are given in Table 1.

The absence of a  $4.40\mu\text{m}$  feature due to aromatic C-D leads to an upper limit on D/H in the aromatic material:

$$\left(\frac{\text{D}}{\text{H}}\right)_{\text{arom.}} < K \times \frac{[F_{\text{arom.CD}}^{\text{corr}}]_{\text{up.lim.}}}{F_{\text{arom.CH}}^{\text{corr}}} = K \times \frac{F_{\text{arom.CH}}^{\text{clip}}}{F_{\text{arom.CH}}} \times \frac{[F_{\text{arom.CD}}^{\text{corr}}]_{\text{up.lim.}}}{F_{\text{arom.CH}}^{\text{clip,corr}}} \quad . \quad (13)$$

where we may use the same  $K$  as defined in Equation (9). Taking  $K \approx 1.2$  and estimating  $F_{\text{arom.CH}}^{\text{clip}} \approx 0.71 F_{\text{arom.CH}}$  (see Figure 5), the upper limits on  $F_{\text{arom.CD}}^{\text{corr}}$  in Table 1 yield upper limits  $(\text{D}/\text{H})_{\text{arom.}} < 0.006$  in SW-Strip,1, and  $(\text{D}/\text{H})_{\text{arom.}} < 0.007$  in NE-Strip (see Table 3). D-enrichment of the aliphatic material exceeds that of the aromatic material by at least a factor 20 in these regions.

Similarly, Figure 11 shows  $4.2 - 4.6\mu\text{m}$  spectra for the Orion Bar and M17, with upper limits for the strength of any  $4.40\mu\text{m}$  feature. Limits on  $(\text{D}/\text{H})_{\text{arom.}}$  in the Orion Bar and M17 are given in Table 3.

### 5.8. Upper Limits on the Nitrile CN Stretching Mode

The Orion Bar spectra appear to have a broad emission feature centered near  $\sim 4.35\mu\text{m}$ , tentatively identified by Peeters et al. (2024) as the CN stretch in nitrile ( $-\text{C}\equiv\text{N}$ ) groups. However, Boersma

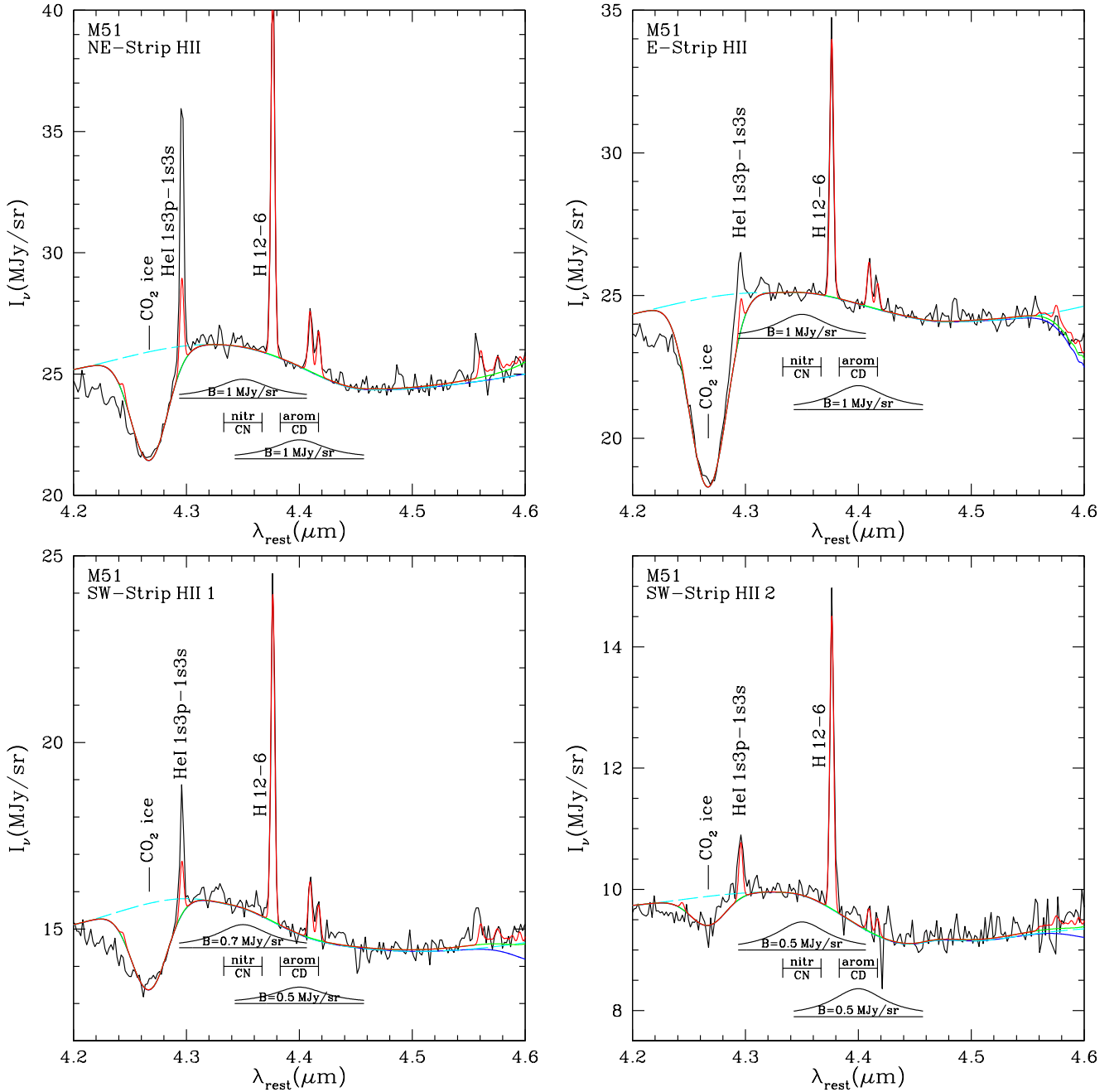


**Figure 10.** The 4.2 – 4.6  $\mu\text{m}$  spectra of the four sightlines in Figure 2. Black curves: observed spectra. Cyan dashed curves: estimate of continuum without ice absorption. Green curves: continuum with ice absorption applied. Red curves: continuum plus emission lines of H, He, and  $\text{H}_2$  (see text). The expected wavelengths for nitrile CN ( $\sim 4.35 \mu\text{m}$ ) and aromatic C–D ( $\sim 4.40 \mu\text{m}$ ) are indicated. In the M51 spectra, there is no evidence of nitrile CN emission or aromatic C–D emission; the inset profile shows our estimated upper limit on the strength of either feature.

et al. (2023) studied seven Galactic regions, including the M17 PDR, and noted that there was little evidence of a nitrile emission feature near the expected wavelength of  $\sim 4.35 \mu\text{m}$ . Similarly, our M51 spectra (see Figure 10) show no evidence of an emission feature near  $4.35 \mu\text{m}$ .

If we assume the FWHM of the  $4.35 \mu\text{m}$  nitrile CN stretch to be similar to the  $0.06 \mu\text{m}$  FWHM expected for the aromatic C–D stretch (see the sample profiles in Figures 10 and 11), the upper bound



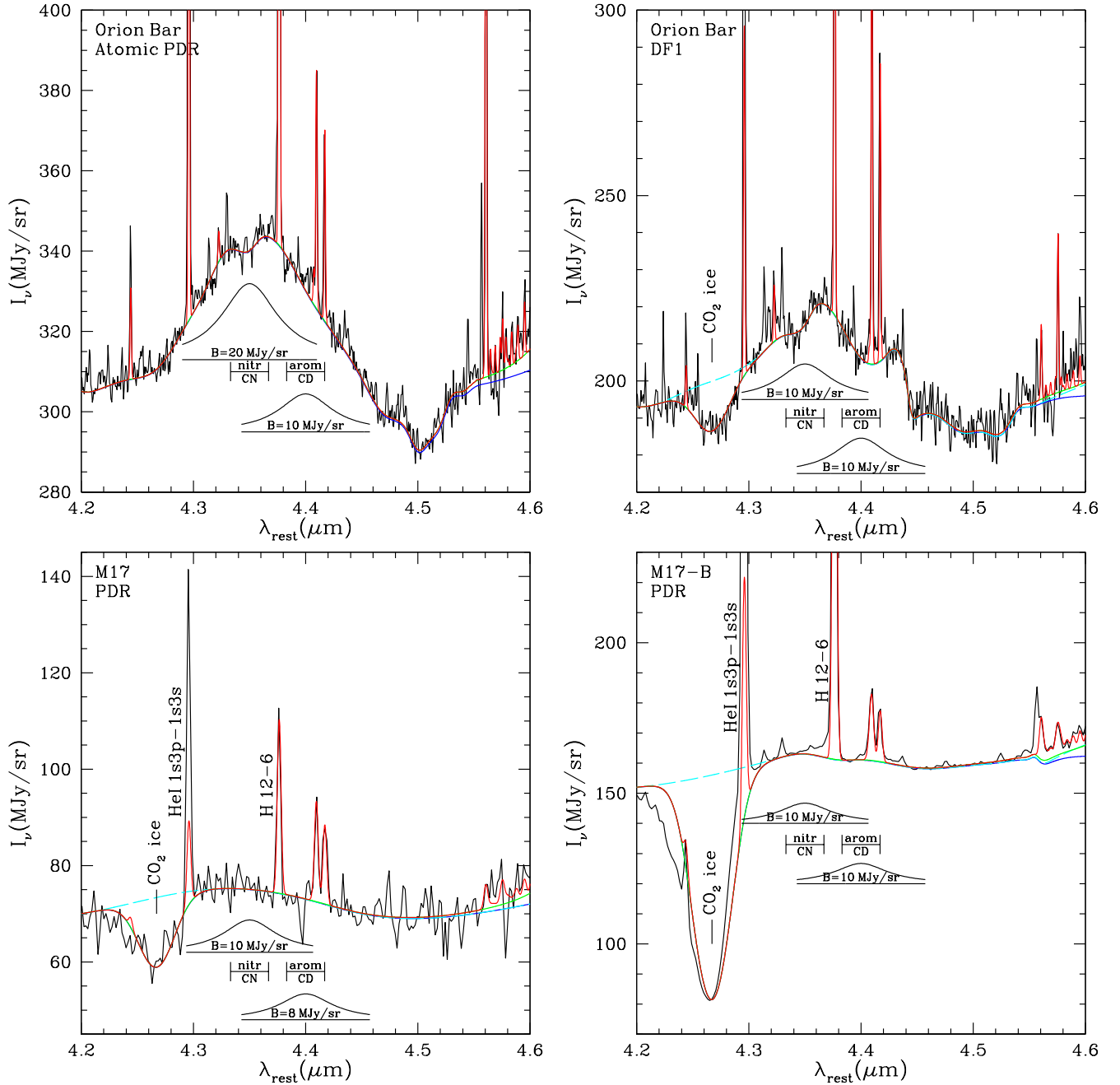


**Figure 11.** Same as Figure 10, but for two positions in the Orion Bar (Peeters et al. 2024) and two positions in M17 (Boersma et al. 2023).

on the power in the nitrile CN stretch is similar to the upper bound estimated for the aromatic C–D stretch.

### 5.9. Upper Limits on a $4.75\mu\text{m}$ Feature

Doney et al. (2016) reported a feature at  $4.75\mu\text{m}$ , with  $\text{FWHM} = 0.047\mu\text{m}$  in Akari spectra of 6 Galactic H II regions, which they attributed to the symmetric aliphatic CD stretching mode. We do not see evidence of this feature in our spectra of H II regions in M51. Figure 7 shows, for each spectrum, a  $4.75\mu\text{m}$  feature that would have been detectable, and which we take as an upper limit

on the feature strength. We find  $F_{4.75\mu\text{m}}^{\text{corr}}/F_{\text{arom.CH}}^{\text{corr}} < 0.004$  for M51 NE-Strip H II, and  $< 0.011$  for all four regions in M51, below the values found by [Doney et al. \(2016\)](#), which ranged from 0.011 for M8, to 0.12 for M17b.

The Orion Bar spectra are more complex (see Figure 8). [Peeters et al. \(2024\)](#) reported detection of the feature in Orion, but in our reanalysis of their data we only claim upper limits (see Table 2). We estimate  $F_{4.75\mu\text{m}}/F_{\text{arom.CH}} < 0.003$  for the atomic PDR, and  $< 0.004$  for DF1.

### 5.10. Model Limitations

At the  $D = 7.5$  Mpc distance of M51 ([Csörnyei et al. 2023](#)), our  $1''.5$  diameter extraction corresponds to 55 pc. With the observed emission originating from a number of subregions within the beam, characterized by different foreground material, the assumption of a uniform screen of dust is unrealistic. However, differential extinction over the  $4 - 5\mu\text{m}$  spectral range considered here is small, so that inaccuracies in modeling the dust extinction are not expected to be important for studying the  $4.65\mu\text{m}$  emission feature. The presence of the XCN ice absorption feature on some sightlines (most prominently in the M51 E-Strip spectrum) does, however, introduce uncertainty.

Uncertainties also arise from the treatment of CO absorption. It is unrealistic to assume a single column density  $N_{\text{CO},v=0}$  between us and the emitting  $v = 1$  CO, with the absorbing CO having a Gaussian velocity distribution with  $b = 3 \text{ km s}^{-1}$ , but with the  $v = 1$  CO sufficiently shifted in velocity so that emission is not absorbed by the  $v = 0$  CO. Failure of the model to accurately reproduce the weak CO emission or absorption features is unsurprising.

### 5.11. Sequestration of Deuterium from the Gas Phase

[Friedman et al. \(2023\)](#) obtained accurate measurements of  $(\text{D}/\text{H})_{\text{gas}}$  on 16 Galactic sightlines, with median  $(\text{D}/\text{H})_{\text{gas}} \approx 17$  ppm, corresponding to  $\text{D}_{\text{dust}}/\text{H}_{\text{total}} \approx 6$  ppm sequestered in the dust. Two sightlines had  $(\text{D}/\text{H})_{\text{gas}} < 9$  ppm, implying  $\text{D}_{\text{dust}}/\text{H}_{\text{total}} > 14$  ppm.

In the diffuse interstellar medium, the carbon in dust grains amounts to  $\text{C}_{\text{dust}}/\text{H}_{\text{total}} \approx 126 \pm 56$  ppm ([Jenkins 2009](#); [Hensley & Draine 2021](#)). The degree of hydrogenation is uncertain but must be appreciable, given observation of the  $3.4\mu\text{m}$  aliphatic C–H stretch in absorption on diffuse ISM sightlines.

Let  $f_{\text{aliph.C}}$  be the fraction of the C atoms that are in aliphatic ( $-\text{CH}_2-$ ) form, and let

$$\phi_{\text{aliph.}} \equiv \left( \frac{\text{D}}{\text{H} + \text{D}} \right)_{\text{aliph.}} \quad (14)$$

be the deuterated fraction for the aliphatic material. For the four regions observed in M51 we estimate  $(\text{D}/\text{H})_{\text{aliph.}} = 0.17 \pm 0.02$ , i.e.,  $\phi_{\text{aliph.}} \approx 0.15 \pm 0.02$ , for the nanoparticles contributing to the emission at  $\lambda < 5\mu\text{m}$ .

With two hydrogens per aliphatic C, the total D sequestered in dust is

$$\frac{\text{D}_{\text{dust}}}{\text{H}_{\text{total}}} = 2f_{\text{aliph.C}} \langle \phi_{\text{aliph.}} \rangle \times \frac{\text{C}_{\text{dust}}}{\text{H}_{\text{total}}} \quad (15)$$

$$= 14 \text{ ppm} \left( \frac{f_{\text{aliph.C}}}{0.2} \right) \left( \frac{\langle \phi_{\text{aliph.}} \rangle}{0.3} \right) \left( \frac{\text{C}_{\text{dust}}/\text{H}_{\text{total}}}{120 \text{ ppm}} \right), \quad (16)$$

where  $\langle \phi_{\text{aliph.}} \rangle$  is averaged over *all* of the aliphatic material, including that in the larger grains. The aliphatic fraction  $f_{\text{aliph.C}}$  is uncertain, but the strength of the  $3.4\mu\text{m}$  absorption observed in the diffuse ISM ([Chiar et al. 2013](#); [Hensley & Draine 2020](#)) requires  $f_{\text{aliph.C}} \approx 0.3(2.5 \times 10^{-18} \text{ cm}/A_{3.4\mu\text{m}})$ , with band strengths  $A_{3.4\mu\text{m}}$  in the range  $(0.5 - 5) \times 10^{-18} \text{ cm}$  estimated for various cations and neutrals (see, e.g., [Yang et al. 2017](#)). For  $f_{\text{aliph.C}} \approx 0.2$  and  $\langle \phi_{\text{aliph.}} \rangle > 0.15$ , the aliphatic hydrocarbons in the interstellar dust population can account for the typical levels of “missing D” in the nearby interstellar medium, while  $\langle \phi_{\text{aliph.}} \rangle = 0.3$  would account for the highest observed levels of “missing D”.

### 5.12. Detectability of Aliphatic C-D in Absorption

The  $4.65\mu\text{m}$  feature may be detectable in absorption on diffuse ISM sightlines with large  $A_V$ . We estimate

$$\left[ \int d\lambda^{-1} \Delta\tau \right]_{4.65} = \frac{\langle \phi_{\text{aliph.}} \rangle}{1 - \langle \phi_{\text{aliph.}} \rangle} \frac{A_{\text{CD}}}{A_{\text{CH}}} \left[ \int d\lambda^{-1} \Delta\tau \right]_{3.42}, \quad (17)$$

where  $A_{\text{CD}}/A_{\text{CH}} \approx 1/1.75$  (Bauschlicher et al. 1997). With  $A_V \approx 10.2$  mag (Torres-Dodgen et al. 1991) and  $[\int d\lambda^{-1} \Delta\tau]_{3.42} = 3.90 \text{ cm}^{-1} \text{ mag}$  (Hensley & Draine 2020) toward Cyg OB-12, we estimate

$$\left[ \int d\lambda^{-1} \Delta\tau \right]_{4.65} \approx 0.22 \text{ cm}^{-1} \frac{\langle \phi_{\text{aliph.}} \rangle}{1 - \langle \phi_{\text{aliph.}} \rangle} \left( \frac{A_V}{\text{mag}} \right), \quad (18)$$

and central optical depth

$$(\Delta\tau)_{4.65\mu\text{m}} \approx 0.011 \frac{\langle \phi_{\text{aliph.}} \rangle}{1 - \langle \phi_{\text{aliph.}} \rangle} \left( \frac{0.0265\mu\text{m}}{\text{FWHM}} \right) \left( \frac{A_V}{\text{mag}} \right). \quad (19)$$

If  $\langle \phi_{\text{aliph.}} \rangle \approx 0.3$ , JWST NIRSpec observations on heavily reddened diffuse ISM sightlines may be able to detect the  $4.65\mu\text{m}$  aliphatic CD stretch in absorption.

## 6. SUMMARY

Our principal conclusions are as follows:

1. The spectra of four massive star-forming regions in M51 include an emission feature near  $4.65\mu\text{m}$  attributed to emission in the aliphatic C–D stretching mode in PAH-related hydrocarbon nanoparticles.
2. The observed aliphatic C–D emission can be approximated by a Drude profile (Equation (3)) with  $\lambda_{\text{aliph.CD}} \approx 4.647\mu\text{m}$ , and  $\text{FWHM} \approx 0.0265\mu\text{m}$ .
3. In the four regions of M51 studied here, the power in the aliphatic C–D emission feature ranges from 12% to 18% of the power in the “clipped” estimate of the  $3.37 - 3.60\mu\text{m}$  nonaromatic C–H emission – 2 to 3 times the fraction found in the Orion Bar PDR. Evidently, the aliphatic material in PAH-related hydrocarbon nanoparticles in M51 is 2 to 3 times more deuterated than in the Orion Bar. For reasonable assumptions concerning the temperature of the emitting nanoparticles, the aliphatic emitters in M51 have  $\langle \text{D/H} \rangle_{\text{aliph.}} \approx 0.17 \pm 0.02$  – enrichment by a factor  $\sim 10^4$  relative to the overall D/H in the ISM.
4. Nondetection of deuterated aromatic emission near  $4.40\mu\text{m}$  leads to upper limits on deuteration of the aromatic material. We find  $(\text{D/H})_{\text{arom.}} < 0.006$  in M51 SW-Strip,1, and  $< 0.003$  in the Orion Bar atomic PDR. D enrichment of the aliphatic material exceeds that of the aromatic material by at least a factor 20.
5. None of the four positions in M51 show evidence of nitrile C–N emission at  $4.35\mu\text{m}$ . We estimate an upper limit  $F_{4.35\mu\text{m}}/F_{\text{arom.CH}} < 0.014$  for all four positions in M51.
6. None of the four positions in M51 show evidence of the  $4.75\mu\text{m}$  emission feature seen in AKARI spectra of Galactic H II regions (Doney et al. 2016). We estimate upper limits  $F_{4.75\mu\text{m}}/F_{\text{arom.CH}} < 0.011$  for all four positions in M51.

7. The ISM in M51 has O/H close to solar (Croxall et al. 2015). With similar degrees of “as-tration”, D/H in M51 is presumed to be close to that in the solar neighborhood. Differences in aliphatic deuteration among regions in M51, and relative to M17 and the Orion Bar, must result from different environmental conditions experienced by the hydrocarbon nanoparticles.
8. The aliphatic deuteration is found to anticorrelate with  $\text{He}^+/\text{H}^+$  in the associated H II (see Figure 9b). Harder and more intense FUV radiation from more massive stars may act to more rapidly de-deuterate the nanoparticles in PDRs near these stars.
9. The depletions of D observed in the diffuse ISM can be accounted for if all of the aliphatic material in dust is as deuterated as observed for the nanoparticles in M51,
10. The  $4.65\mu\text{m}$  aliphatic CD stretch may be detectable in absorption on sightlines to Galactic stars with large  $A_V$ .

The JWST data presented in this Letter were obtained from the MAST at the Space Telescope Science Institute. The JWST observations analyzed can be accessed via [doi:10.17909/k6kg-nc75](https://doi.org/10.17909/k6kg-nc75). These observations are associated with JWST program 3435.

We thank G. DelZanna, V. J. Esposito and Aigen Li for helpful discussions. We especially thank P. J. Storey for kindly making available extended tables of H I emissivities. We thank the anonymous referee for a thoughtful and very helpful report that led to improvements in the paper.

This work is based on observations made with the NASA/ESA/CSA James Webb Space Telescope. The data were obtained from the Mikulski Archive for Space Telescopes at the Space Telescope Science Institute, which is operated by the Association of Universities for Research in Astronomy, Inc., under NASA contract NAS 5-03127 for JWST. These observations are associated with GO program #3435. The authors acknowledge the PDRs4All Team for their publicly available data products from the Early Release Science Program #1288. We also used publicly available data for M17 from Cycle 1 GO Program 1591, PI L. Allamandola. Support for program GO #3435 was provided by NASA through a grant from the Space Telescope Science Institute, which is operated by the Association of Universities for Research in Astronomy, Inc., under NASA contract NAS 5-03127.

This research has made use of NASA’s Astrophysics Data System, as well as ds9, a tool for data visualization supported by the Chandra X-ray Science Center (CXC) and the High Energy Astrophysics Science Archive Center (HEASARC) with support from the JWST Mission office at the Space Telescope Science Institute for 3D visualization.

K.S., D.D., J.D.S., A.D.B., M.L.B., D.C., K.D.G., A.K.L., J.R.D., and B.F.W. acknowledge support from grant JWST-GO-03435. A.A. acknowledges support from the Swedish National Space Agency (SNSA) through the grant 2021-00108. R.S.K. acknowledges financial support from the European Research Council via the ERC Synergy Grant “ECOGAL” (project ID 855130), from the German Excellence Strategy via the Heidelberg Cluster of Excellence (EXC 2181-390900948) “STRUCTURES”, and from the German Ministry for Economic Affairs and Climate Action in project “MAINN” (funding ID 50002206). R.S.K. is grateful for computing resources provided by the Ministry of Science, Research and the Arts (MWK) of the State of Baden-Württemberg through bwHPC and the German Science Foundation (DFG) through grants INST 35/1134-1 FUGG and 35/1597-1 FUGG, and also for data storage at SDS@hd funded through grants INST 35/1314-1 FUGG and INST 35/1503-1 FUGG.

## REFERENCES

- |  |  |
|--|--|
| <p>Allamandola, L. J. 1993, in <i>Astronomical Society of the Pacific Conference Series</i>, Vol. 41, <i>Astronomical Infrared Spectroscopy: Future Observational Directions</i>, ed. S. Kwok, 197</p> | <p>Allamandola, L. J., Boersma, C., Lee, T. J., Bregman, J. D., &amp; Temi, P. 2021, <i>ApJL</i>, 917, L35, doi: <a href="https://doi.org/10.3847/2041-8213/ac17f0">10.3847/2041-8213/ac17f0</a></p> |
|--|--|

- Allamandola, L. J., Sandford, S. A., Tielens, A. G. G. M., & Herbst, T. M. 1992, *ApJ*, 399, 134, doi: [10.1086/171909](https://doi.org/10.1086/171909)
- Allamandola, L. J., Tielens, A. G. G. M., & Barker, J. R. 1985, *ApJL*, 290, L25
- . 1989, *ApJS*, 71, 733
- Argyriou, I., Glasse, A., Law, D. R., et al. 2023, *A&A*, 675, A111, doi: [10.1051/0004-6361/202346489](https://doi.org/10.1051/0004-6361/202346489)
- Bauschlicher, C. W., Langhoff, S. R., Sandford, S. A., & Hudgins, D. M. 1997, *Journal of Physical Chemistry A*, 101, 2414, doi: [10.1021/jp963740w](https://doi.org/10.1021/jp963740w)
- Blagrave, K. P. M., Martin, P. G., Rubin, R. H., et al. 2007, *ApJ*, 655, 299, doi: [10.1086/510151](https://doi.org/10.1086/510151)
- Boersma, C., Allamandola, L. J., Esposito, V. J., et al. 2023, *ApJ*, 959, 74, doi: [10.3847/1538-4357/ad022b](https://doi.org/10.3847/1538-4357/ad022b)
- Böker, T., Arribas, S., Lützgendorf, N., et al. 2022, *A&A*, 661, A82, doi: [10.1051/0004-6361/202142589](https://doi.org/10.1051/0004-6361/202142589)
- Boulanger, F., Onaka, T., Pilleri, P., & Joblin, C. 2011, in *EAS Publications Series*, Vol. 46, *EAS Publications Series*, ed. C. Joblin & A. G. G. M. Tielens (Cambridge, UK: Cambridge Univ. Press), 399–405, doi: [10.1051/eas/1146041](https://doi.org/10.1051/eas/1146041)
- Chandra, S., Maheshwari, V. U., & Sharma, A. K. 1996, *A&AS*, 117, 557
- Chiar, J. E., Tielens, A. G. G. M., Adamson, A. J., & Ricca, A. 2013, *ApJ*, 770, 78, doi: [10.1088/0004-637X/770/1/78](https://doi.org/10.1088/0004-637X/770/1/78)
- Croxall, K. V., Pogge, R. W., Berg, D. A., Skillman, E. D., & Moustakas, J. 2015, *ApJ*, 808, 42, doi: [10.1088/0004-637X/808/1/42](https://doi.org/10.1088/0004-637X/808/1/42)
- Csörnyei, G., Anderson, R. I., Vogl, C., et al. 2023, *A&A*, 678, A44, doi: [10.1051/0004-6361/202346971](https://doi.org/10.1051/0004-6361/202346971)
- Del Zanna, G., & Storey, P. J. 2022, *MNRAS*, 513, 1198, doi: [10.1093/mnras/stac800](https://doi.org/10.1093/mnras/stac800)
- Doney, K. D., Candian, A., Mori, T., Onaka, T., & Tielens, A. G. G. M. 2016, *A&A*, 586, A65, doi: [10.1051/0004-6361/201526809](https://doi.org/10.1051/0004-6361/201526809)
- Draine, B. T. 2004, in *Origin and Evolution of the Elements*, ed. A. McWilliam & M. Rauch (Cambridge, UK: Cambridge Univ. Press), 317–335
- Draine, B. T. 2006, in *Astr. Soc. Pac. Conf. Ser.* 348, *Astrophysics in the Far Ultraviolet*, ed. G. Sonneborn, H. W. Moos, & B.-G. Andersson, Vol. 348, 58–69
- Draine, B. T. 2011, *Physics of the Interstellar and Intergalactic Medium* (Princeton, NJ: Princeton Univ. Press)
- Draine, B. T., & Li, A. 2001, *ApJ*, 551, 807, doi: [10.1086/320227](https://doi.org/10.1086/320227)
- Draine, B. T., Li, A., Hensley, B. S., et al. 2021, *ApJ*, 917, 3, doi: [10.3847/1538-4357/abff51](https://doi.org/10.3847/1538-4357/abff51)
- Esposito, V. J., Fortenberry, R. C., Boersma, C., Maragkoudakis, A., & Allamandola, L. J. 2024, *MNRAS*, 531, L87, doi: [10.1093/mnras/rlae037](https://doi.org/10.1093/mnras/rlae037)
- Friedman, S. D., Chayer, P., Jenkins, E. B., et al. 2023, *ApJ*, 946, 34, doi: [10.3847/1538-4357/acbcbf](https://doi.org/10.3847/1538-4357/acbcbf)
- García-Rojas, J., Esteban, C., Peimbert, A., et al. 2007, *RMxAA*, 43, 3, doi: [10.48550/arXiv.astro-ph/0610065](https://doi.org/10.48550/arXiv.astro-ph/0610065)
- Gardner, J. P., Mather, J. C., Abbott, R., et al. 2023, *PASP*, 135, 068001, doi: [10.1088/1538-3873/acd1b5](https://doi.org/10.1088/1538-3873/acd1b5)
- Gibb, E. L., Whittet, D. C. B., Boogert, A. C. A., & Tielens, A. G. G. M. 2004, *ApJS*, 151, 35, doi: [10.1086/381182](https://doi.org/10.1086/381182)
- Gordon, K. D., Clayton, G. C., Decleir, M., et al. 2023, *ApJ*, 950, 86, doi: [10.3847/1538-4357/accb59](https://doi.org/10.3847/1538-4357/accb59)
- Hensley, B. S., & Draine, B. T. 2020, *ApJ*, 895, 38, doi: [10.3847/1538-4357/ab8cc3](https://doi.org/10.3847/1538-4357/ab8cc3)
- . 2021, *ApJ*, 906, 73, doi: [10.3847/1538-4357/abc8f1](https://doi.org/10.3847/1538-4357/abc8f1)
- Hudgins, D. M., Bauschlicher, Jr., C. W., & Sandford, S. A. 2004, *ApJ*, 614, 770
- Jakobsen, P., Ferruit, P., Alves de Oliveira, C., et al. 2022, *A&A*, 661, A80, doi: [10.1051/0004-6361/202142663](https://doi.org/10.1051/0004-6361/202142663)
- Jenkins, E. B. 2009, *ApJ*, 700, 1299, doi: [10.1088/0004-637X/700/2/1299](https://doi.org/10.1088/0004-637X/700/2/1299)
- Jenkins, E. B., Tripp, T. M., Woźniak, P. R., Sofia, U. J., & Sonneborn, G. 1999, *ApJ*, 520, 182, doi: [10.1086/307447](https://doi.org/10.1086/307447)
- Jura, M. 1982, in *NASA Conference Publication*, Vol. 2238, *Advances in Ultraviolet Astronomy: Four Years of IUE Research*, ed. Y. Kondo, 54–60
- Lacy, J. H., Sneden, C., Kim, H., & Jaffe, D. T. 2017, *ApJ*, 838, 66, doi: [10.3847/1538-4357/aa6247](https://doi.org/10.3847/1538-4357/aa6247)
- Lai, T. S. Y., Smith, J. D. T., Baba, S., Spoon, H. W. W., & Imanishi, M. 2020, *ApJ*, 905, 55, doi: [10.3847/1538-4357/abc002](https://doi.org/10.3847/1538-4357/abc002)
- Leger, A., & Puget, J. L. 1984, *A&A*, 137, L5



- Linsky, J. L., Draine, B. T., Moos, H. W., et al. 2006, *ApJ*, 647, 1106
- Martins, F., Schaerer, D., & Hillier, D. J. 2005, *A&A*, 436, 1049, doi: [10.1051/0004-6361:20042386](https://doi.org/10.1051/0004-6361:20042386)
- Mori, T., Onaka, T., Sakon, I., et al. 2022, *ApJ*, 933, 35, doi: [10.3847/1538-4357/ac71ae](https://doi.org/10.3847/1538-4357/ac71ae)
- Öberg, K. I., Boogert, A. C. A., Pontoppidan, K. M., et al. 2011, *ApJ*, 740, 109, doi: [10.1088/0004-637X/740/2/109](https://doi.org/10.1088/0004-637X/740/2/109)
- Onaka, T., Sakon, I., & Shimonishi, T. 2022, *ApJ*, 941, 190, doi: [10.3847/1538-4357/ac9b15](https://doi.org/10.3847/1538-4357/ac9b15)
- Peeters, E., Allamandola, L. J., Bauschlicher, Jr., C. W., et al. 2004, *ApJ*, 604, 252
- Peeters, E., Habart, E., Berné, O., et al. 2024, *A&A*, 685, A74, doi: [10.1051/0004-6361/202348244](https://doi.org/10.1051/0004-6361/202348244)
- Pogge, R. W., Owen, J. M., & Atwood, B. 1992, *ApJ*, 399, 147, doi: [10.1086/171910](https://doi.org/10.1086/171910)
- Smith, L. J., Norris, R. P. F., & Crowther, P. A. 2002, *MNRAS*, 337, 1309, doi: [10.1046/j.1365-8711.2002.06042.x](https://doi.org/10.1046/j.1365-8711.2002.06042.x)
- Storey, P. J., & Hummer, D. G. 1995, *MNRAS*, 272, 41
- Tielens, A. G. G. M. 2008, *ARA&A*, 46, 289, doi: [10.1146/annurev.astro.46.060407.145211](https://doi.org/10.1146/annurev.astro.46.060407.145211)
- Torres-Dodgen, A. V., Tapia, M., & Carroll, M. 1991, *MNRAS*, 249, 1
- van Broekhuizen, F. A., Keane, J. V., & Schutte, W. A. 2004, *A&A*, 415, 425, doi: [10.1051/0004-6361:20034161](https://doi.org/10.1051/0004-6361:20034161)
- Van Kerckhoven, C., Tielens, A. G. G. M., & Waelkens, C. 2002, *A&A*, 384, 568, doi: [10.1051/0004-6361:20011814](https://doi.org/10.1051/0004-6361:20011814)
- Verstraete, L., Puget, J. L., Falgarone, E., et al. 1996, *A&A*, 315, L337
- Yang, X. J., & Li, A. 2023a, *ApJS*, 268, 12, doi: [10.3847/1538-4365/ace4c6](https://doi.org/10.3847/1538-4365/ace4c6)
- . 2023b, *ApJS*, 268, 50, doi: [10.3847/1538-4365/acebe6](https://doi.org/10.3847/1538-4365/acebe6)
- Yang, X. J., Li, A., & Glaser, R. 2020, *ApJS*, 251, 12, doi: [10.3847/1538-4365/abba28](https://doi.org/10.3847/1538-4365/abba28)
- Yang, X. J., Li, A., Glaser, R., & Zhong, J. X. 2017, *ApJ*, 837, 171, doi: [10.3847/1538-4357/aa5fa9](https://doi.org/10.3847/1538-4357/aa5fa9)
- Yeh, T.-H., Olive, K. A., & Fields, B. D. 2021, *JCAP*, 2021, 046, doi: [10.1088/1475-7516/2021/03/046](https://doi.org/10.1088/1475-7516/2021/03/046)

## APPENDIX

## CO LINES IN ABSORPTION

Let  $N_{\text{CO}}(v, J)$  be the column density of  $\text{CO}(v, J)$ . The line-center optical depth in an absorption line is

$$\tau_0 = \frac{1}{8\pi^{3/2}} \frac{2J_u + 1}{2J_\ell + 1} A_{ul} \frac{\lambda_{u\ell}^3 N(v_\ell, J_\ell)}{b} \quad (1)$$

$$= 2.78 \frac{(2J_u + 1)/3}{(2J_\ell + 1)/1} \left( \frac{A_{ul}}{11.5 \text{ s}^{-1}} \right) \left( \frac{\lambda_{u\ell}}{4.7576 \mu\text{m}} \right)^3 \left( \frac{N(v_\ell, J_\ell)}{10^{16} \text{ cm}^{-2}} \right) \left( \frac{3 \text{ km s}^{-1}}{b} \right), \quad (2)$$

where  $b$  is the usual Doppler-broadening parameter. The correction for stimulated emission is neglected because (1) the population in the  $v = 1$  levels is small, and (2) the velocity distribution of the  $v = 1$  CO is likely to differ from that of the  $v = 0$  CO. Because the cold CO is likely at a different velocity than the hot  $v = 1$  CO, we do not apply CO absorption to the CO emission lines.

The dimensionless equivalent width in the absorption line is taken to be (Draine 2011, Eq. 9.27)

$$W \approx \sqrt{\pi} \frac{b}{c} \frac{\tau_0}{1 + \tau_0/(2\sqrt{2})} \quad \text{for } \tau_0 \leq 1.25393 \quad (3)$$

$$\approx \frac{2b}{c} \left[ \ln \left( \frac{\tau_0}{\ln 2} \right) \right]^{1/2} \quad \text{for } \tau_0 > 1.25393 \quad (4)$$

The JWST spectra do not resolve the absorption line. Let  $R \equiv \lambda/\text{FWHM}_\lambda$  be the resolution of the spectrograph. For  $N(\text{CO}) \lesssim 10^{17} \text{ cm}^{-2}$  and  $b \approx 3 \text{ km s}^{-1}$ , we have  $\tau_0 \lesssim 30$  and  $W \lesssim 4 \times 10^{-5}$ . If  $W \ll 1/R$  (as will be the case for JWST resolution  $R \lesssim 3000$ ), the attenuation due to the line is

$$\alpha(\lambda) = \frac{W}{\sqrt{2\pi} \sigma} e^{-(\lambda - \lambda_{u\ell})^2 / 2\sigma_\lambda^2}, \quad (5)$$

where  $\sigma = 1/(R\sqrt{8 \ln 2})$ , and  $\sigma_\lambda = \lambda/(R\sqrt{8 \ln 2})$ .